

# Probabilistic Quantification of Tsunami Currents in Karachi Port, Makran Subduction Zone, using Statistical Emulation

Devaraj Gopinathan<sup>1</sup>, Mohammad Heidarzadeh<sup>2</sup>, and Serge Guillas<sup>1</sup>

<sup>1</sup>University College London

<sup>2</sup>Brunel University London

November 30, 2022

## Abstract

In this paper, we model the full range of possible local impacts of future tsunamis in the Makran subduction zone (MSZ) at Karachi port, Pakistan. For the first time, the 3-D subduction geometry Slab2 is employed in the MSZ, in conjunction with the most refined rupture segmentation to date for this region, to improve the earthquake source definition. Motivated by the massive sediment layer over the MSZ, we also introduce to tsunami modeling the application of the sediment amplification formula, resulting in enhancements of seabed deformation up to 60% locally. Furthermore, we design a new unstructured mesh algorithm for our GPU-accelerated tsunami code in order to efficiently represent flow velocities, including vortices, down to a resolution of 10m in the vicinity of the port. To afford to compute very large number of high resolution tsunami scenarios, for the granularity and extent of the range of magnitudes (occurrence ratios of 1:100,000 implied by the Gutenberg-Richter relation) and locations of source, we create a statistical surrogate i.e. emulator) of the tsunami model. Our main contribution is hence the largest set of emulated predictions using any realistic tsunami code to date: 1 million per location. We go on to obtain probabilistic representations of maximum tsunami velocities and heights at around 200 locations in the port area of Karachi. Amongst other findings, we discover substantial local variations of currents and heights. Hence we argue that an end-to-end synthesis of advanced physical, numerical and statistical modeling is instrumental to comprehensively model local impacts of tsunamis.

1           **Probabilistic Quantification of Tsunami Currents in**  
2           **Karachi Port, Makran Subduction Zone, using**  
3           **Statistical Emulation**

4           **Devaraj Gopinathan<sup>1</sup>, Mohammad Heidarzadeh<sup>2</sup>, Serge Guillas<sup>1</sup>**

5           <sup>1</sup>Department of Statistical Science, University College London, Gower Street, London WC1E 6BT, UK.  
6           <sup>3</sup>Department of Civil & Environmental Engineering, Brunel University London, Uxbridge UB8 3PH, UK.

7           **Key Points:**

- 8           • The first emulation of a tsunami model at 10 *m* resolution and largest emulation  
9           of a tsunami model with 1 million scenarios  
10          • The first use of sediment amplification and Slab2 subduction geometry in tsunami  
11          modeling for Makran Subduction Zone  
12          • The first areawide probabilistic hazard maps of tsunami currents for Karachi port  
13          extracted from 1 million scenarios

---

Corresponding author: Devaraj Gopinathan, [d.gopinathan@ucl.ac.uk](mailto:d.gopinathan@ucl.ac.uk)

## 14 Abstract

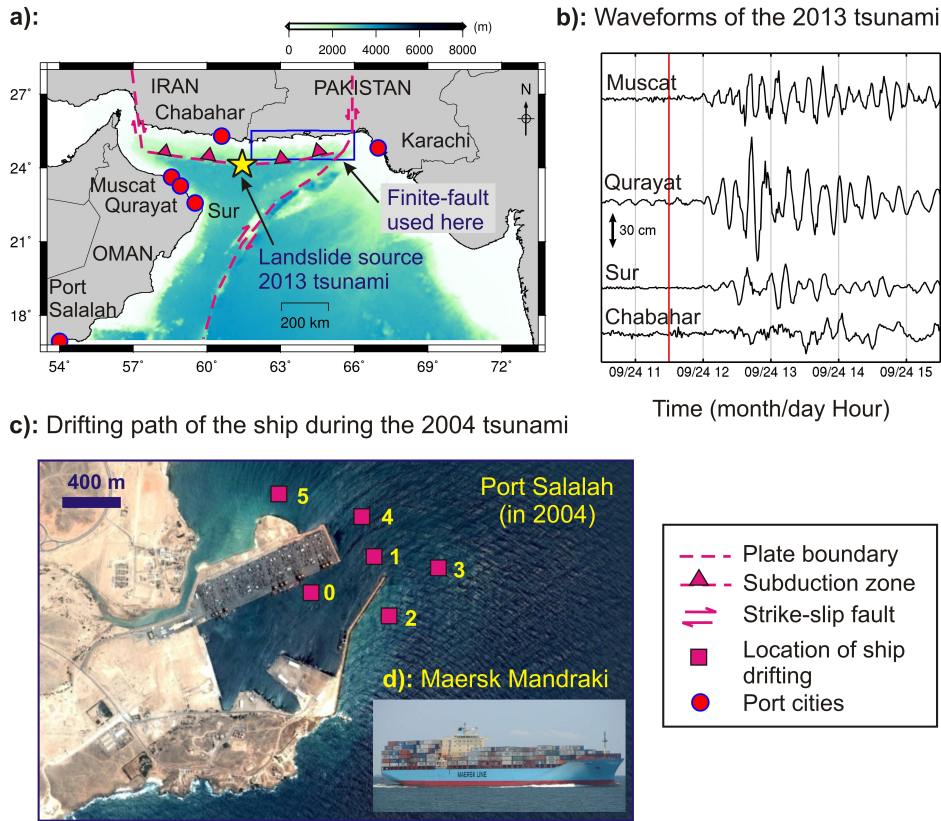
15 In this paper, we model the full range of possible local impacts of future tsunamis  
 16 in the Makran subduction zone (MSZ) at Karachi port, Pakistan. For the first time, the  
 17 3-D subduction geometry Slab2 is employed in the MSZ, in conjunction with the most  
 18 refined rupture segmentation to date for this region, to improve the earthquake source  
 19 definition. Motivated by the massive sediment layer over the MSZ, we also introduce to  
 20 tsunami modeling the application of the sediment amplification formula, resulting in en-  
 21 hancements of seabed deformation up to 60 % locally. Furthermore, we design a new un-  
 22 structured mesh algorithm for our GPU-accelerated tsunami code in order to efficiently  
 23 represent flow velocities, including vortices, down to a resolution of 10 *m* in the vicin-  
 24 ity of the port. To afford to compute very large number of high resolution tsunami sce-  
 25 narios, for the granularity and extent of the range of magnitudes (occurrence ratios of  
 26 1 : 100,000 implied by the Gutenberg-Richter relation) and locations of source, we cre-  
 27 ate a statistical surrogate (*i.e.* emulator) of the tsunami model. Our main contribution  
 28 is hence the largest set of emulated predictions using any realistic tsunami code to date:  
 29 1 million per location. We go on to obtain probabilistic representations of maximum tsunami  
 30 velocities and heights at around 200 locations in the port area of Karachi. Amongst other  
 31 findings, we discover substantial local variations of currents and heights. Hence we ar-  
 32 gue that an end-to-end synthesis of advanced physical, numerical and statistical mod-  
 33 eling is instrumental to comprehensively model local impacts of tsunamis.

## 34 Plain Language Summary

35 Ports are under great risk from tsunamis. Recent events show how violent currents  
 36 can unmoor and steer vessels into port structures. We model possible future currents and  
 37 heights of tsunamis in Karachi port, Pakistan. We also create an advanced definition of  
 38 the earthquake source taking into account the layer of sediments in the seabed near the  
 39 coast of Makran. A high resolution tsunami numerical model is employed to represent  
 40 currents. We mimic the numerical model by a statistical model in order to produce 1 mil-  
 41 lion tsunami events of local impact. We are able to conclude which areas of the port are  
 42 much more likely to be affected by intense currents, and by how much.

## 43 1 Introduction

44 Following the unexpected damage incurred at ports from the tsunamis of 2004 (In-  
 45 dian Ocean), 2010 (Chile) and 2011 (Japan) (Borrero, Lynett, & Kalligeris, 2015; Okal  
 46 et al., 2006), it is of paramount importance to investigate the associated hazard. Ports  
 47 are vital economic lifelines and thus need to be safeguarded from natural disasters to pre-  
 48 vent *e.g.* a sudden interruption of trade and commerce, a halt in the flow of essential com-  
 49 modities, as well as the destruction of livelihoods of fishermen communities. Despite re-  
 50 cent studies (Borrero, Goring, et al., 2015; Borrero, Lynett, & Kalligeris, 2015; Lynett  
 51 et al., 2012, 2014) and advances in high-fidelity modeling (Lynett et al., 2017), proba-  
 52 bilistic methods tackling the quantification of future tsunami hazard due to strong flows  
 53 in harbors are absent. The need for such probabilistic quantifications is further accen-  
 54 tuated by certain peculiarities that were observed with the phenomena of tsunami cur-  
 55 rents in ports. On 26 December 2004, the Sumatra-Andaman (SA) tsunami waves at the  
 56 Omani port of Salalah wrested the freighter *Maersk Mandraki* from the main wharf be-  
 57 fore it was shoved around by the vortices induced from the tsunami currents (Okal et  
 58 al., 2006). The 285 *m* long ship drifted uncontrollably for hours, despite manual inter-  
 59 vention (Figure 1). It looped both inside and outside the harbor prior to winding up on  
 60 a sand bar. Another anomaly was observed on 24 September 2013, when a submarine  
 61 landslide in the Makran subduction zone (MSZ) generated a tsunami in the North-Western  
 62 (NW) Indian Ocean, affecting the coasts of Oman, Iran, Pakistan and India (Heidarzadeh  
 63 & Satake, 2014). The landslide that caused the tsunami was the secondary effect of a



69

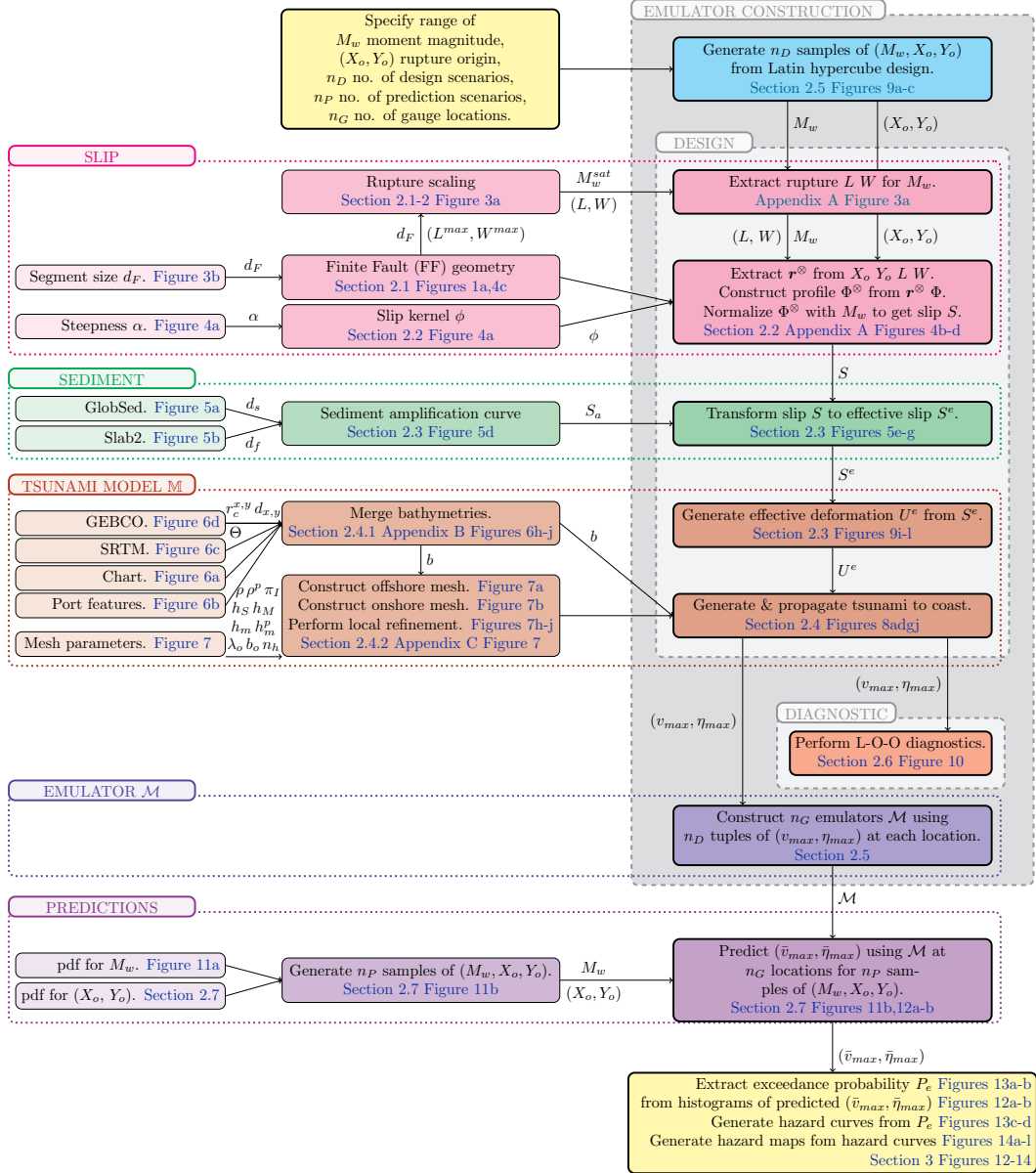
70 **Figure 1.** a) The Makran subduction zone area showing Karachi port studied in this work.  
 71 b) Waveforms of the tsunami generated by a submarine landslide in the Makran region on 24  
 72 September 2013 based on Heidarzadeh and Satake (2014, Figure 11). c) Drifting of a large ship,  
 73 the *Mearsk Mandraki* (shown in panel d) within the port of Salalah (pink squares) following the  
 74 December 2004 Indian Ocean tsunami based on the data by Okal et al. (2006). The numbers  
 75 to the right of each point indicate the sequence in which the ship drifted. d) The ship *Mearsk*  
 76 *Mandraki* which was drifting in port Salalah following the 2004 Indian Ocean tsunami.

64 small  $M_w$  7.7 inland strike-slip earthquake. Tide-gauge records displayed tsunami waves  
 65 of small amplitude ( $20 \pm 7$  cm) in the affected regions, except for three Omani ports (Heidarzadeh  
 66 & Satake, 2014, Table 1 & Figure 3). Relatively larger amplitudes were found in the ports  
 67 of Muscat (51 cm), Quarayat (109 cm) and Sur (40 cm). Here, the waves also prevailed  
 68 for a relatively longer duration ( $\approx 6$  h) compared to the other ports (Figure 1).

77 Overall, the above case from the 2004 tsunami provides evidence of the treacherous  
 78 nature of tsunami currents in harbors. Although it may seem rational to associate  
 79 high wave amplitudes with high velocities, the arresting feature is that the strong cur-  
 80 rents continued for hours after the waves with maximum amplitude had arrived (nearly  
 81 9 h in Salalah). This is all the more consequential since conventional tsunami warnings  
 82 may be lifted after visibly perceptible signs of the tsunami (*i.e.* vertical displacement)  
 83 have disappeared, whereas the strong currents may manifest later on. In the case of the  
 84 2013 Makran tsunami also, it is highly probable that the coastal geometry and local bathymetry  
 85 were responsible for long tsunami oscillations.

90 The Makran Subduction Zone (MSZ) has given rise to tsunamis in 1945 (Byrne et  
 91 al., 1992; Heidarzadeh et al., 2008) and 2013 (Heidarzadeh & Satake, 2014). Recent stud-





86

87 **Figure 2.** Global workflow describing the integration of different work components in this  
 88 study for emulation-based probabilistic assessment of hazard for tsunami currents and heights in  
 89 the port.

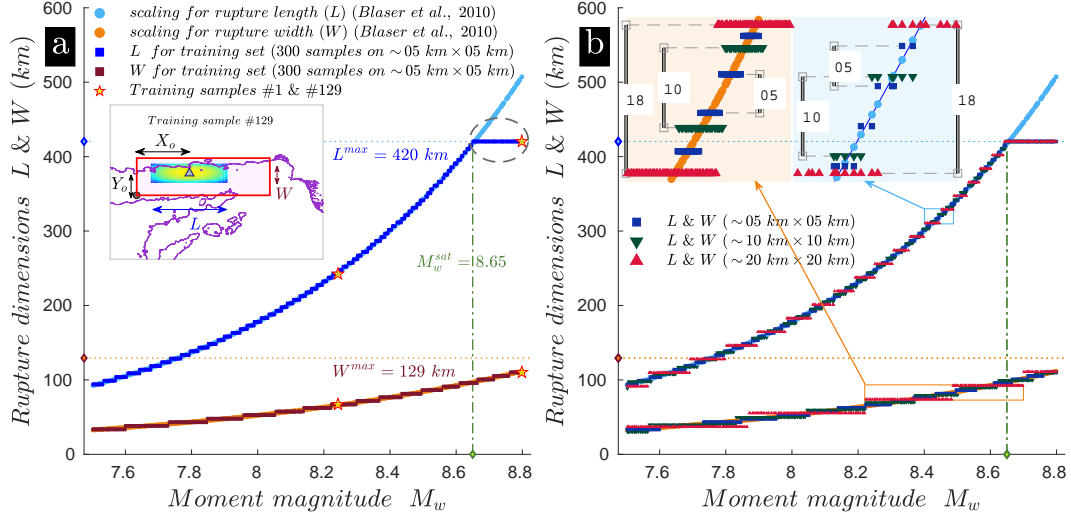
ies estimate the megathrust potential for the eastern part of the MSZ (blue rectangle, Figure 1) to be  $M_w$  8.8 – 9.0 (Smith et al., 2013). Given the peculiarities observed in Makran ports during the 2004 and 2013 tsunamis, there is a pressing need for a comprehensive quantification of tsunami hazard, and associated uncertainties, especially port velocities. However, the accurate simulation of tsunami currents at shallow depths requires accurate coastline definition, high resolution bathymetry, and highly refined meshes, over enough time to capture the maximum. Thus, in this study we employ spatial resolutions of 10 m for coastline, 30 m for bathymetry, and 10 m for the computational mesh, locally in the vicinity of Karachi port (Pakistan), for a total simulation time of 12 hours. The large number of runs, at such resolutions, needed for probabilistic hazard assessments stretches the limit of current High-performance Computing facilities, even with the latest GPU (Graphics Processing Unit) acceleration (Reguly et al., 2018). In terms of the seabed deformation given as input to the tsunami model, we introduce here an earthquake source designed with segments of size 5 km  $\times$  5 km with carefully constructed positive slip kernels to preserve fidelity to both magnitude scaling (Blaser et al., 2010) and slip scaling relations (Allen & Hayes, 2017). Second, the presence of a considerable sediment layer over the Makran Subduction Zone (MSZ) (up to 2 km) demands incorporation of its influence on the deformation, since a remarkable amplification of up to 60 % can be generated (Dutykh & Dias, 2010).

We select a probabilistic route in order to quantify uncertainties in future tsunamis due to the uncertain earthquake source variations (see the full workflow in Figure 2). However, since the probability of large events is small, a comprehensive coverage of the Gutenberg-Richter relation requires a large number of runs for the diversity of plausible events to be well represented across magnitudes and source location (in the thousands at minimum for a coarse quantification and much more for realistic assessments). Due to the considerable computational complexity of each high-resolution tsunami simulation of coastal tsunami currents, such a probabilistic endeavor can only be achieved by replacing the numerical tsunami model by a statistical surrogate: the emulator. To our knowledge, this is the first time that emulation has been marshalled to generate future earthquake-generated tsunami currents; it has been employed only once in the past for currents, for a single source of landslide-generated tsunamis with huge benefits in terms of computational costs and hazard assessment (Salmanidou et al., 2019). With a design of only 300 runs, we fit an emulator to produce 1 million plausible tsunamis at any location. These emulated runs enable us to fully characterize uncertainty in future tsunami currents. Section 2 describes the models and methods used in this work, Section 3 discusses the results, and conclusions are drawn in Section 4.

## 2 Models, Data and Methods

In this section, we describe the finite fault apparatus (Section 2.1), construction of the slip profile on the finite fault (Section 2.2), integration of the sediment amplification over the slips (Section 2.3), tsunami propagation (Section 2.4), merging of bathymetries at different resolutions (Section 2.4.1), design of algorithm for locally refined unstructured mesh (Section 2.4.2), emulator training (Section 2.5), emulator diagnostics (Section 2.6) and finally the hazard predictions for 1 million events (Section 2.7). The global workflow is displayed in Figure 2.

There are formidable computational challenges that must be addressed in order to accurately represent both the actual geophysical processes and their uncertainties. Often, in tsunami modeling this trade-off between capability and capacity in High Performance Computing (HPC) is left unresolved by either radically simplifying the physics (*e.g.* a linear tsunami propagation till say 100 m depth with the use of an empirical relationship thereafter), or running only a few high resolution simulations as scenarios. We argue that our tsunami emulation framework, in this context of currents that are highly nonlinear and very sensitive to near shore bathymetry, provides a solution to this trade-



150

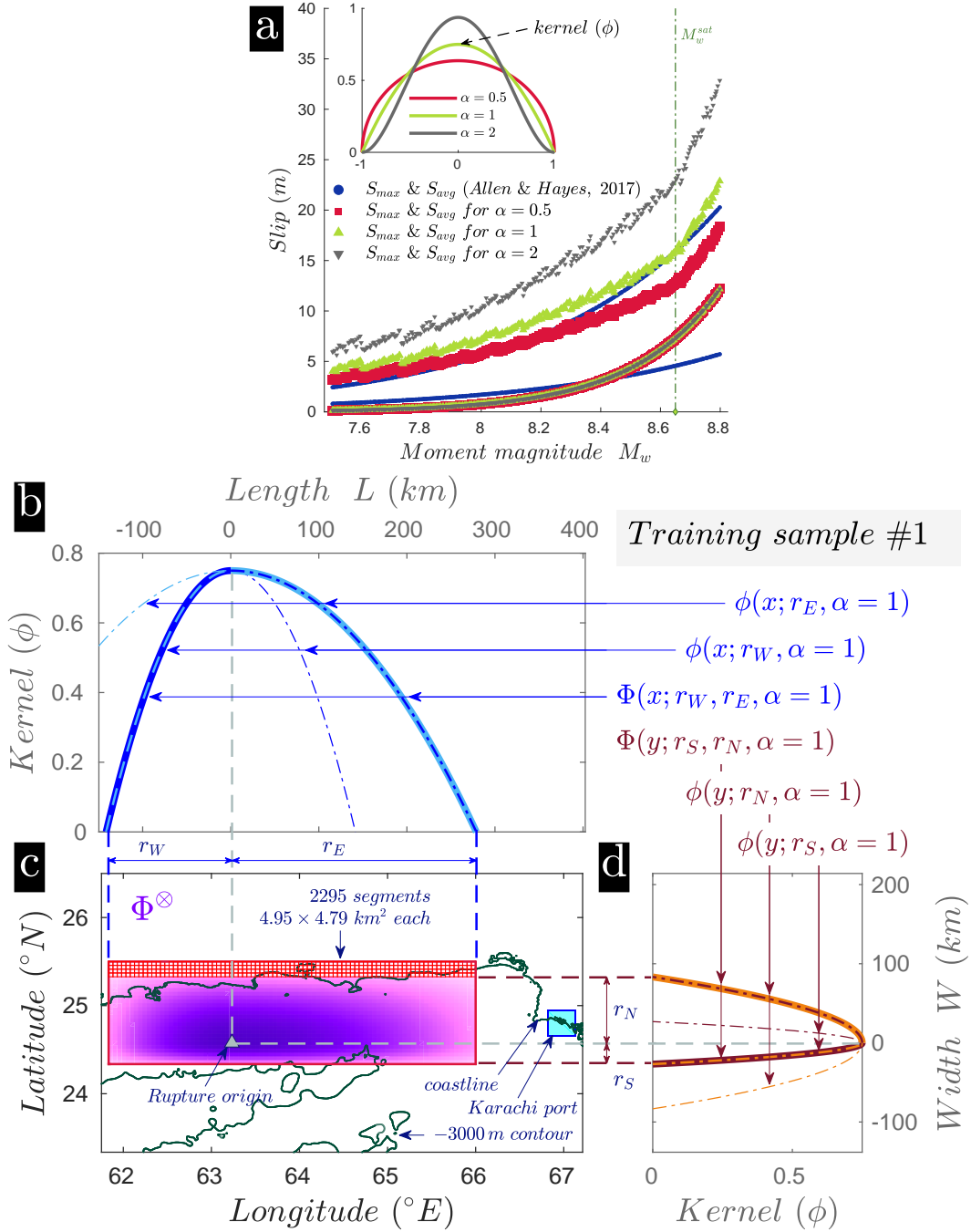
151 **Figure 3.** Finite fault model. a) Scaling relation of rupture length ( $L$ ) and width ( $W$ ) with  
 152 respect to the rupture moment magnitude ( $M_w$ ) showing the maximum length ( $L^{max}$ ), width  
 153 ( $W^{max}$ ) and moment magnitude ( $M_w^{sat}$ ) accommodable in the eastern MSZ. The lengths and  
 154 widths of 300 earthquake scenarios are plotted over the scaling relation for an FF model made  
 155 up of  $\sim 5 \text{ km} \times 5 \text{ km}$  segments. The rupture length saturates after  $M_w 8.65$  (green line) in the  
 156 region marked by the ellipse. The inset plot display the rupture dimensions ( $L, W$ ) and rupture  
 157 origin co-ordinates ( $X_o, Y_o$ ) on a sample scenario (no. 129). Sample nos. 1 and 129 are marked  
 158 on the scaling curves. b) Same as (a) but also includes FF models made up of  $\sim 5 \text{ km} \times 5 \text{ km}$ ,  
 159  $\sim 10 \text{ km} \times 10 \text{ km}$  and  $\sim 20 \text{ km} \times 20 \text{ km}$  segments. The inset plots zoom on to the scaling  
 160 relation to reveal discontinuities in the realizable fault dimensions.

144 off between precision and coverage of uncertainties. It requires manipulation of very large  
 145 data sets on HPC, as well as complex post-processing on diverse software and data plat-  
 146 forms. Thus, our work here is at the forefront of what can be achieved using the most  
 147 refined finite fault segmentation, the latest tsunami model acceleration schemes on GPU  
 148 clusters, hierarchical file formats, smart unstructured meshes and newest multi-threading  
 149 emulation platforms.

## 161 2.1 Finite Fault Model

162 We construct a finite fault (FF) on the eastern section of MSZ (blue rectangle, Fig-  
 163 ure 1) using a total number ( $n_F$ ) of 2295 rectangular segments (Figures 4c & 9j). The  
 164 overall dimension of the FF model is  $420 \text{ km} \times 129 \text{ km}$  ( $L^{max} \times W^{max}$ ). The slip on a  
 165 segment is denoted by  $S_i$ , where  $i$  varies from 1 to 2295. The closed-form equations from  
 166 Okada (1985) transform the slips and other FF parameters into a static vertical displace-  
 167 ment denoted by  $U$  (calculated inside an uplift calculation box, see Figures 9g & h). The  
 168 final vertical displacement field results from the combined superposition of vertical dis-  
 169 placements due to all the activated fault segments. Among the FF parameters, the dip  
 170 angle and fault depth ( $d_f$ ) are sourced from the recent plate boundary model, Slab2 (Hayes  
 171 et al., 2018; Hayes, 2018). The strike and rake angles are kept constant at  $270^\circ$  and  $90^\circ$ .

178 Each segment size ( $d_F$ ) is approximately  $5 \text{ km} \times 5 \text{ km}$  ( $l_i \times w_i$ ). All the segments  
 179 are arrayed in an  $85 \times 27$  grid. This resolution is chosen to preserve fidelity to the scal-  
 180 ing relation from Blaser et al. (2010) (Figure 3a), arrived through comparing the per-  
 181 formance of different segment sizes *viz.*  $5 \text{ km} \times 5 \text{ km}$ ,  $10 \text{ km} \times 10 \text{ km}$  and  $20 \text{ km} \times 20 \text{ km}$



172

173 **Figure 4.** Slip profile generation. a) Validating maximum slips ( $S_{max}$ ) and average slips  
 174 ( $S_{avg}$ ) for 300 earthquake scenarios as per the scaling relation in Allen and Hayes (2017) by vary-  
 175 ing the steepness ( $\alpha$ ) b) & d) Bi-lobed kernels  $\Phi(x; r_E, r_W, \alpha)$  and  $\Phi(y; r_S, r_N, \alpha)$  along fault  
 176 length and width respectively for a sample scenario (no. 1). c) Tensor product  $\Phi^{\otimes}$  of the two  
 177 bi-lobed kernel functions in (b) and (d) prior to magnitude normalization.

(Figure 3b). The discrepancy to the scaling relation appears as discontinuities in the realizable fault lengths ( $L$ ) and widths ( $W$ ) (Figure 3a inset). The size of the discontinuities are the same as the resolution chosen (Figure 3b inset). Thus, we observe the least discontinuity while using a  $5\text{ km} \times 5\text{ km}$  segmentation (Figure 3). We use the definitions of the seismic moment  $M_w$  and moment magnitude  $M_0$  (Kanamori, 1977; Hanks & Kanamori, 1979) as,

$$M_w = (2/3) (\log_{10} M_0 - 9.1), \quad M_0 = \sum_{i=1}^{n_F} \mu l_i w_i S_i \quad (1)$$

with  $\mu = 3 \times 10^{10} \text{ N/m}^2$  being the modulus of rigidity. Our implementation of the Okada suite is adapted from the dMODELS code (Battaglia et al., 2012, 2013). The next section details the design of the slip profile over the FF model.

## 2.2 Slip Profile Generation

Slips are usually modeled to be uniform on the FF segments, even though inversions of seismic sources evidenced localised concentrations of high slips or asperities over a backdrop of lower slips (Grezio et al., 2017). To generate a similar behaviour in our slip profiles, we utilize a positive kernel function  $\phi$  having a functional form (Figure 4a inset):

$$\phi(x; r, \alpha) = \begin{cases} c_\alpha \left(1 - \left|\frac{x}{r}\right|^2\right)^\alpha & |x| \leq r \\ 0 & |x| > r \end{cases} \quad (2)$$

where  $c_\alpha = \frac{\Gamma(2l+2)}{2^{2l+1}\Gamma(l+1)^2}$  is the normalizing constant made up of the gamma function ( $\Gamma$ ), the length scale  $r$  defines the domain where  $\phi$  is non-zero and the parameter  $\alpha$  adjusts the steepness of  $\phi$ . Using  $\phi$  as the core, we construct the bi-lobed kernel function  $\Phi$ :

$$\Phi(x; r_l, r_r, \alpha) = \begin{cases} \phi(x; r_l, \alpha) & -r_l \leq x \leq 0 \\ \phi(x; r_r, \alpha) & 0 \leq x \leq r_r \end{cases} \quad (3)$$

where  $r_l$  and  $r_r$  are the length scales of the left and right lobes of  $\Phi$ , their values depending on the position of the rupture origin ( $X_o, Y_o$ ) with respect to the fault length ( $L$ ) and width ( $W$ ) (Figures 3a inset & 4b-d). The tensor product of the two bi-lobed kernel functions, one along the length (Figure 4b) and another along the width (Figure 4d) of the fault yields the surface  $\Phi^\otimes$  (Figure 4c):

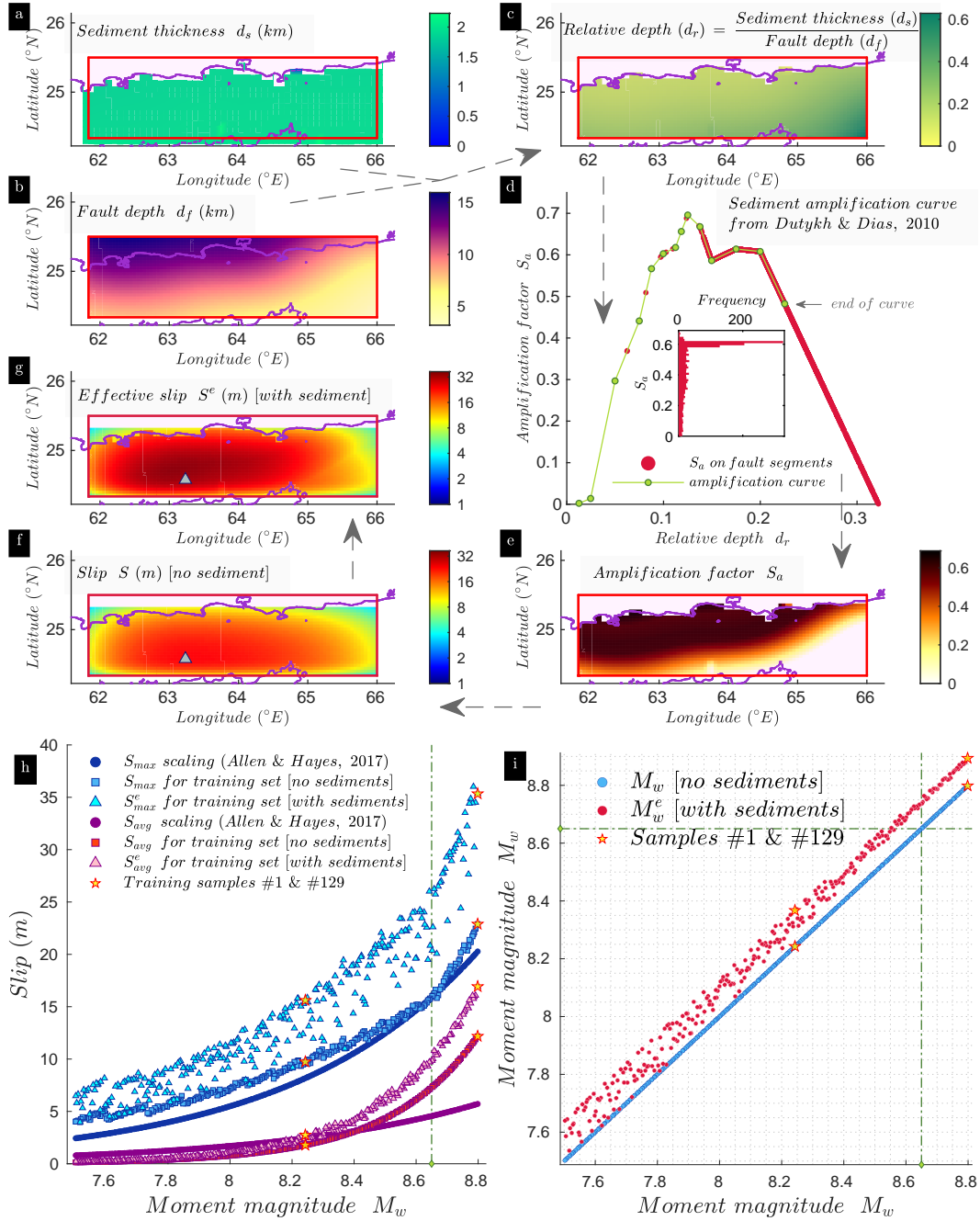
$$\Phi^\otimes(x, y; \mathbf{r}^\otimes, \alpha) = \Phi(x; r_W, r_E, \alpha) \otimes \Phi(y; r_S, r_N, \alpha) \quad (x, y) \in [-r_W, r_E] \times [-r_S, r_N] \quad (4)$$

where  $[-r_W, r_E] \times [-r_S, r_N]$  denotes the domain of the rupture and  $\mathbf{r}^\otimes = \{r_W, r_E, r_S, r_N\}$ . A normalization of  $\Phi^\otimes$  with the required moment magnitude on the rupture yields the final slip profile  $S$  (Figure 5f and 9e & f). The algorithm for the above construction is detailed in Appendix A. Given the algorithm, we arrive at  $\alpha = 1$  by varying  $\alpha$  to closely match the maximum slip  $S_{max}$  and average slip  $S_{avg}$  curves generated from the scaling relations in Allen and Hayes (2017, Table 2) (Figure 4a). The next section describes the incorporation of the effect of seafloor sediment layer.

## 2.3 Sediment Amplification

Considerable amplification (up to 60% locally) of crustal deformation due to the presence of layers of sediments on the seafloor was shown in Dutykh and Dias (2010, Figure 12). We introduce it here in tsunami modeling, by making use of the sediment amplification curve (Figure 5d). The curve uses the relative depth ( $d_r^i$ ) of the  $i$ th segment (Figure 5c) calculated as:

$$d_r^i = \frac{d_s^i}{d_f^i} \quad (5)$$



217

218 **Figure 5.** Sediment amplification. a) Sediment thickness  $d_s$  over eastern MSZ. b) Fault depth  
 219  $d_f$ . c) Relative depth  $d_r$ . d) Sediment amplification curve from Dutykh and Dias (2010). The  
 220 inset histogram shows the distribution of  $S_a$  for all the FF segments. e) Sediment amplification  
 221 factor  $S_a$ . f) Slip profile  $S$  without sediments. g) Effective slip profile  $S^e$  incorporating influence  
 222 of sediments. h) Comparison of  $S_{avg}$  and  $S_{max}$  with and without the influence of sediments to  
 223 slip scaling in Allen and Hayes (2017). i) Same as (h) but for moment magnitude with ( $M_w^e$ ) and  
 224 without ( $M_w$ ) the effect of sediments.



232 where  $d_s^i$  is the sediment thickness over the segment interpolated from GlobSed (Straume  
 233 et al., 2019), and  $d_f^i$  is the down-dip fault depth of the segment taken from Slab2 (Hayes  
 234 et al., 2018) (Figures 5a & b). Given  $d_s^i$ , the sediment amplification curve supplies the  
 235 sediment amplification factor ( $S_a^i$ ) on the segment (Figure 5e). The amplification due  
 236 to the sediments is incorporated by multiplying the slip  $S^i$  (Figure 5f) with the sediment  
 237 amplification factor  $S_a^i$  resulting in an effective slip  $S_i^e$  (Figure 5g):

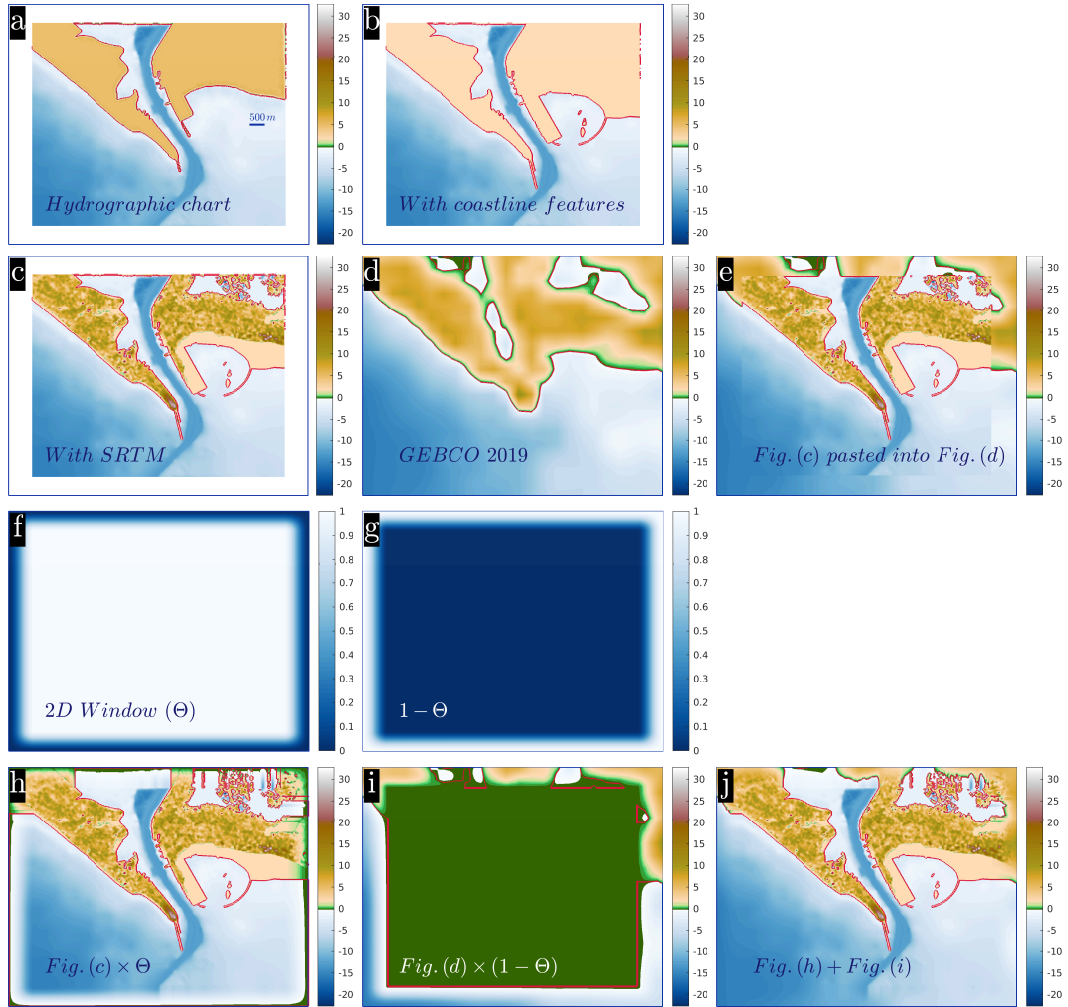
$$238 \quad S_i^e = S_i (1 + S_a^i) \quad (6)$$

239 The closed-form equations from Okada (1985) transform the effective slips  $S_i^e$  into the  
 240 effective vertical displacement  $U^e$  (Figures 9k & l). The influence of sediments not only  
 241 increases the slips but also modifies the profile, as evident in the emergence of a double-  
 242 lobed profile in the effective slip (Figure 5g). The effect is more conspicuous in the as-  
 243 sociated deformations (compare Figures 9g & k). The amplification factor ( $S_a$ ) peaks  
 244 at a relative depth of approximately 0.13 after which it decreases. Given the geometry  
 245 of the fault and overlying sediment profile, a significant number of segments have an am-  
 246 plification factor between 0.4 – 0.6 (or, equivalently a 40 – 60 % amplification) (Figures  
 247 5d inset & e). Furthermore, the sediment amplification factor for the whole MSZ is shown  
 248 in Figure 5e; its value is strongly dominated by the fault depth (Figure 5b) rather than  
 249 the sediment thickness (Figure 5a) which is uniform around 2 km. The sediment ampli-  
 250 fication curve is defined only till a relative depth of 0.23 in Dutykh and Dias (2010). We  
 251 linearly extrapolate the curve in order to be as conservative as possible in the region where  
 252 it is not defined as well as to smoothly transition from regions of higher to lower fault  
 253 depths. The counterparts of average slip  $S_{avg}$  and maximum slip  $S_{max}$  of  $S$  (without sedi-  
 254 ments) are defined as average effective slip  $S_{avg}^e$  and maximum effective slip  $S_{max}^e$  of  $S^e$   
 255 (with sediments). Similarly, effective moment magnitude  $M_w^e$  is defined, by replacing  $S_i$   
 256 with  $S_i^e$  in Eqn. 1. The effect of sediments on slips is compared in Figure 5h. Here, the  
 257 increased scatter of  $S_{max}^e$  compared to  $S_{avg}^e$  is due to the spatial distribution of  $S_a$ , which  
 258 significantly amplifies  $S_{max}^e$  depending on the rupture origin ( $X_o, Y_o$ ). Also, the increase  
 259 in scatter of  $S_{max}^e$  as  $M_w$  decreases is due to the decrease in rupture dimensions that al-  
 260 low many earthquake scenarios to be situated in areas of lower  $S_a$ . This aspect is pro-  
 261 nounced in a similar comparison of  $M_w^e$  to  $M_w$  in Figure 5i. The next section describes  
 262 the propagation of the tsunami resulting from the deformations caused by the effective  
 263 slips.

## 281 2.4 Tsunami Propagation

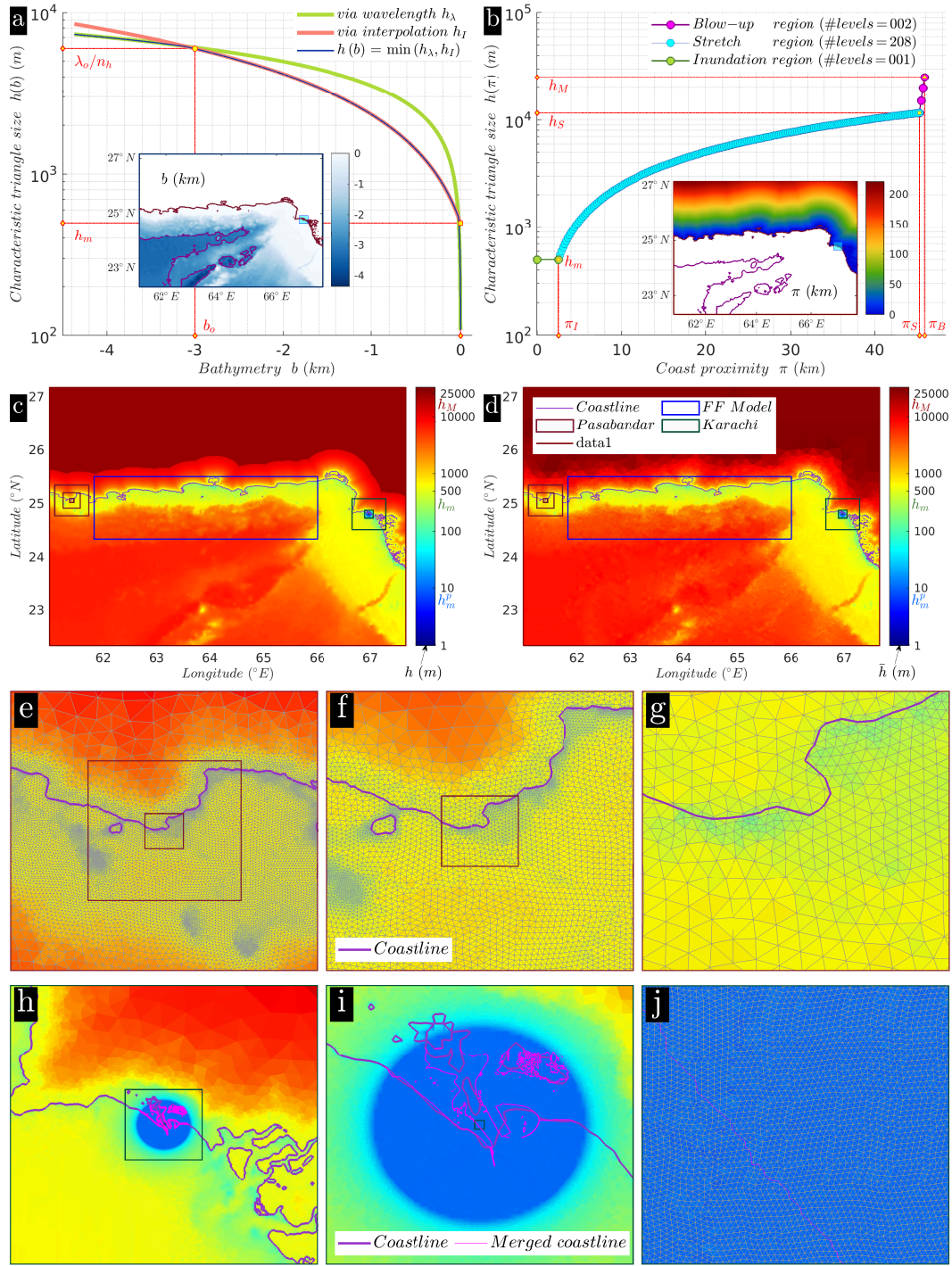
282 Unlike simulations for analysing wave heights which require a few hours of simu-  
 283 lation time, capturing the velocities need a longer simulation time. Thus, each scenario  
 284 is run for 12 h of simulation time ( $T_s$ ) to obtain the maximum tsunami velocity and wave  
 285 height, and therefore is computationally expensive. It is not only imperative that the  
 286 numerical algorithms in the computer code for tsunami simulations run efficiently at fine  
 287 mesh resolutions needed to capture the currents (10 m), but also that the code is amenable  
 288 to adequate parallelisation. Thus, to run 300 such scenarios, we employ VOLNA-OP2  
 289 that has been shown to run efficiently for unstructured meshes on parallel GPUs (Reguly  
 290 et al., 2018). The number of scenarios (*i.e.* 300) is an order of magnitude higher than  
 291 in existing studies (Hasan et al., 2017; Borrero, Goring, et al., 2015; Heidarzadeh & Ki-  
 292 jko, 2011). Usual simulations employ the Green’s functions approach to superpose the  
 293 tsunami wave heights due to a multi-segment finite fault source. Here, we use the the  
 294 Non-linear Shallow Water Equations (NSWEs) to model not only the propagation of the  
 295 tsunami but also the run-up/down process at the coast (Dias et al., 2014). The finite  
 296 volume (FV) cell-centered method for tessellation of control volume is used in VOLNA.  
 297 Thus, the barycentres of the cells are associated with the degrees of freedom. Dutykh  
 298 et al. (2011) and Giles et al. (2020) may be referred for details of numerical implemen-  
 299 tation, validation against standard benchmarks and comprehensive error analysis. VOLNA





264

265 **Figure 6.** Merging of bathymetries. a) Digitized hydrographic chart bathymetry around  
 266 Karachi port. b) Chart data with altered coastline after addition of port features from Google  
 267 Earth. c) Chart data supplemented with SRTM data. d) GEBCO bathymetry around Karachi  
 268 port. e) Merged bathymetry with chart data in (c) pasted into GEBCO bathymetry in (d). f) 2D  
 269 window ( $\Theta$ ). g) Complement of  $\Theta$ , *i.e.* ( $1 - \Theta$ ). h) Chart bathymetry in (c) multiplied by window.  
 270 i) GEBCO bathymetry in (d) multiplied by complement of window. j) Final merged bathymetry  
 271 resulting from addition of windowed bathymetries in (h) and (i).



272

273 **Figure 7.** Localised non-uniform unstructured mesh. a) Mesh-sizing rule for offshore mesh  
 274 based on bathymetry  $b$ , shown in the inset. b) Mesh-sizing rule for onshore mesh based on coast  
 275 proximity  $\pi$ , shown in the inset. c) Mesh sizing function  $h$  supplied to Gmsh for the whole  
 276 domain resulting from the mesh-sizing rules in (a) and (b). d) Actual mesh sizes  $\bar{h}$  in mesh  
 277 generated from Gmsh using the mesh sizing function in (c). e-g) [no local refinement] Mesh at  
 278 Pasabandar shown at scales of  $64 \text{ km} \times 64 \text{ km}$ ,  $32 \text{ km} \times 32 \text{ km}$  and  $8 \text{ km} \times 8 \text{ km}$  respectively. h-j)  
 279 [with local refinement] Mesh at Karachi port shown at scales of  $64 \text{ km} \times 64 \text{ km}$ ,  $16 \text{ km} \times 16 \text{ km}$   
 280 and  $0.5 \text{ km} \times 0.5 \text{ km}$  respectively.

300 models the tsunami life-cycle with:

$$301 \quad \frac{\delta H}{\delta t} + \nabla \cdot (H\mathbf{v}) = 0 \quad (7)$$

$$302 \quad \frac{\delta H\mathbf{v}}{\delta t} + \nabla \cdot \left( H\mathbf{v} \otimes \mathbf{v} + \frac{g}{2} H^2 \mathbf{I}_2 \right) = gH\nabla b \quad (8)$$

304 where  $H(\mathbf{x}, t) = b + \eta$  is the total water depth defined as the sum of free surface ele-  
 305 vation  $\eta(\mathbf{x}, t)$ , and time-dependent bathymetry  $b(\mathbf{x}, t)$ . The two horizontal components  
 306 of the depth-averaged fluid velocity are contained in  $\mathbf{v}(\mathbf{x}, t)$ ,  $g$  is the standard gravity  
 307 and  $\mathbf{I}_2$  is the  $2 \times 2$  identity matrix. The maximum tsunami velocity  $v_{max}$  and wave height  
 308  $\eta_{max}$  at a location  $(\mathbf{x}, t)$  are computed as:

$$309 \quad v_{max}(\mathbf{x}) = \max_{0 < t \leq T_s} \|\mathbf{v}(\mathbf{x}, t)\|_2 \quad (9)$$

$$310 \quad \eta_{max}(\mathbf{x}) = \max_{0 < t \leq T_s} \eta(\mathbf{x}, t) \quad (10)$$

312 The dynamic bathymetry  $b(\mathbf{x}, t)$  is composed as:

$$313 \quad b(\mathbf{x}, t) = b_s(\mathbf{x}) + U^e(\mathbf{x}, t) \quad (11)$$

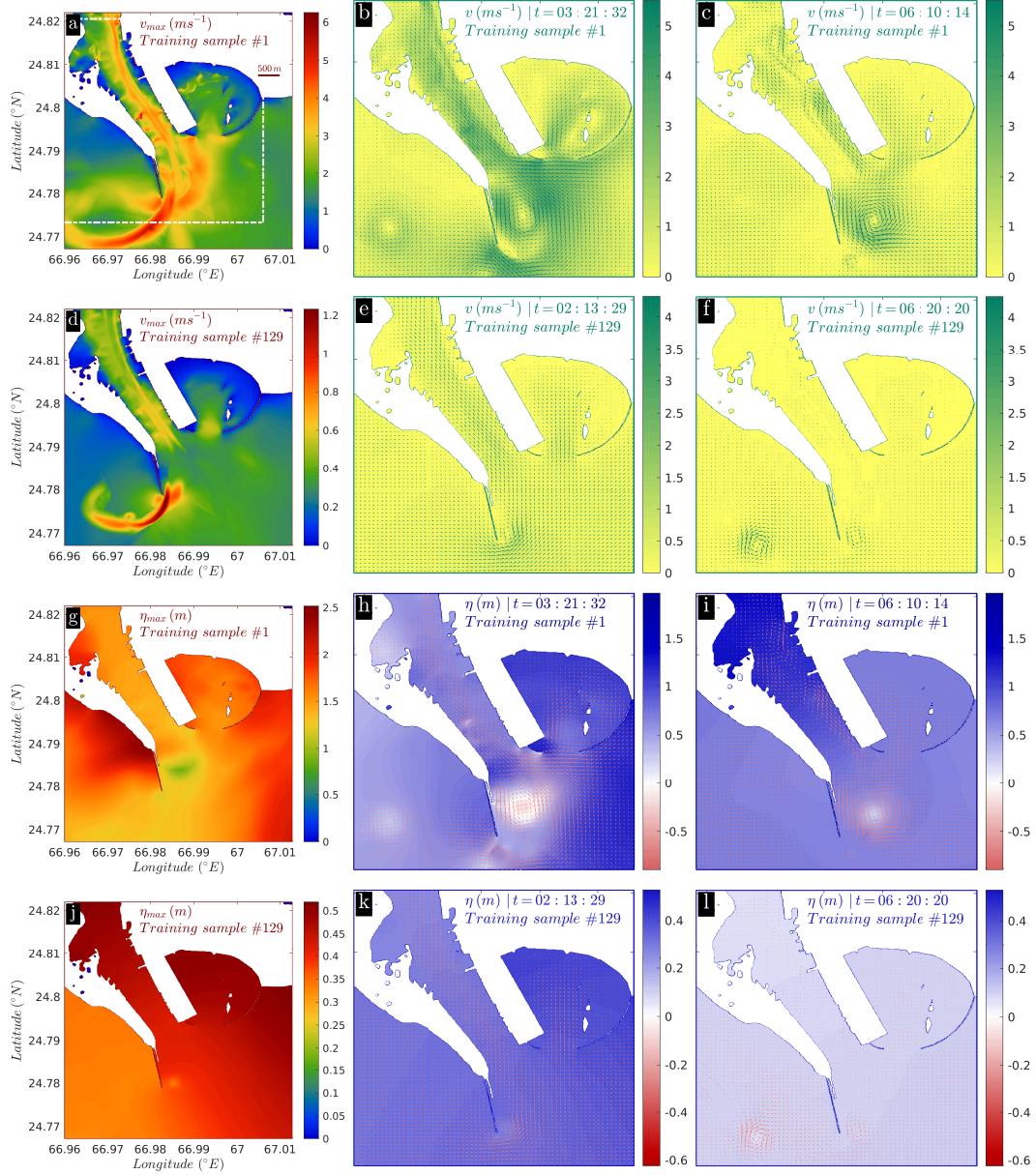
314 where  $b_s$  is the static bathymetry and  $U^e$  is the effective deformation due to the influ-  
 315 ence of sediments (Section 2.3). In this work, an instantaneous rupture is assumed, *i.e.*  
 316  $U^e$  is supplied once at the beginning of the simulation. Further, to reduce the compu-  
 317 tational burden of calculating deformations from 300 ruptures,  $U^e$  is computed only within  
 318 a uplift calculation box covering the rupture (see green rectangle in Figures 9g-h & k-  
 319 l). We now move on the bathymetry  $b_s$  and unstructured mesh, both vital components  
 320 for an accurate modeling of currents in shallow water and near the coast.

#### 321 **2.4.1 Merging of Bathymetries**

322 The bathymetry used for the simulations is sourced from the GEBCO 2019 data  
 323 set (GEBCO Bathymetric Compilation Group 2019, 2019), having a resolution of 15''  
 324 (Figure 6d). Accurate modeling of port velocities and currents near the coast requires  
 325 high resolution bathymetry and good definition of the coastline. Towards this, we use  
 326 digitized bathymetry data at a resolution of  $\sim 30 m$  from hydrographic charts for Karachi  
 327 port (Figure 6a). Further, we correct the shoreline using satellite imagery from Google  
 328 Earth at  $\sim 10 m$  resolution wherever port structures and breakwaters need to be resolved  
 329 (Figure 6b). The charts do not contain topographic data, which we supplement with SRTM  
 330 v3 1'' data (Figure 6c). Simply replacing the GEBCO data with the hydrographic chart  
 331 data gives rise to sharp and unrealistic discontinuities in the merged data set (Figure 6e).  
 332 We ameliorate this by smoothly merging the hydrographic data into the GEBCO data  
 333 by a procedure using cosine-tapered Tukey windows (Figures 6f-g). The detailed algo-  
 334 rithm can be found in Appendix B.

#### 340 **2.4.2 Localised Non-Uniform Unstructured Mesh**

341 We design a customised mesh algorithm for the unstructured mesh sizing function  
 342 in three stages corresponding to offshore, onshore and port regions. A strategy based on  
 343 bathymetry  $b(\mathbf{x})$  is used to generate the mesh in sea (Figure 7a), whilst proximity to  
 344 the coast  $\pi(\mathbf{x})$  is used to size the mesh on land (Figure 7b). We also locally refine the  
 345 mesh to 10 m resolution at Karachi port (Figure 7h-j). This three pronged strategy strikes  
 346 a balance between the fine mesh resolution required near the port for resolution of ve-  
 347 locities and associated overall computational cost. The non-uniform meshes for the sim-  
 348 ulation are generated using Gmsh (Geuzaine & Remacle, 2009). Considering the dimen-  
 349 sions of the finite fault earthquake sources ( $L \times W$ ), we assume an approximate source



335

336 **Figure 8.** Tsunami propagation. a) Maximum velocity  $v_{max}$  around Karachi port over a simulation  
 337 time of 12h for sample no. 1. b-c) Snapshots of velocities  $v$  for sample no. 1 at various  
 338 times restricted to the box (dashed line) in (a). d-f) Same as (a-c) but for sample no. 129.  
 339 Same as (a-f) but for tsunami height  $\eta_{max}$  (and  $\eta$ ).



350 wavelength ( $\lambda_o < \sqrt{L^2 + W^2}$ ) of the tsunami, and a representative ocean depth of the  
 351 Makran trench ( $b_o \sim 3 \text{ km}$ ), and calculate the time period ( $T_\lambda$ ) of the wave as,

$$352 \quad T_\lambda = \lambda_o / \sqrt{g b_o} \quad (12)$$

353 Here,  $\lambda_o = 60 \text{ km}$ , which is around 60 % of the maximum distance contained in the small-  
 354 est rupture considered in this work, *i.e.* of size  $\sim 94 \text{ km} \times 34 \text{ km}$  for a  $M_w 7.5$  event (sam-  
 355 ple no. 300). Next, assuming that the time period of the tsunami is the same everywhere  
 356 in the domain, we get for a depth  $b(\mathbf{x})$  (van Scheltinga et al., 2012),

$$357 \quad \lambda_n / \sqrt{b(\mathbf{x})} = \lambda_o / \sqrt{b_o} \quad (13)$$

358 which in turn relates the characteristic triangle (or element) length  $h_\lambda(b)$  for depth  $b(\mathbf{x})$   
 359 as,

$$360 \quad h_\lambda(b) = (\lambda_o / n_h) \sqrt{b(\mathbf{x}) / b_o} \quad (14)$$

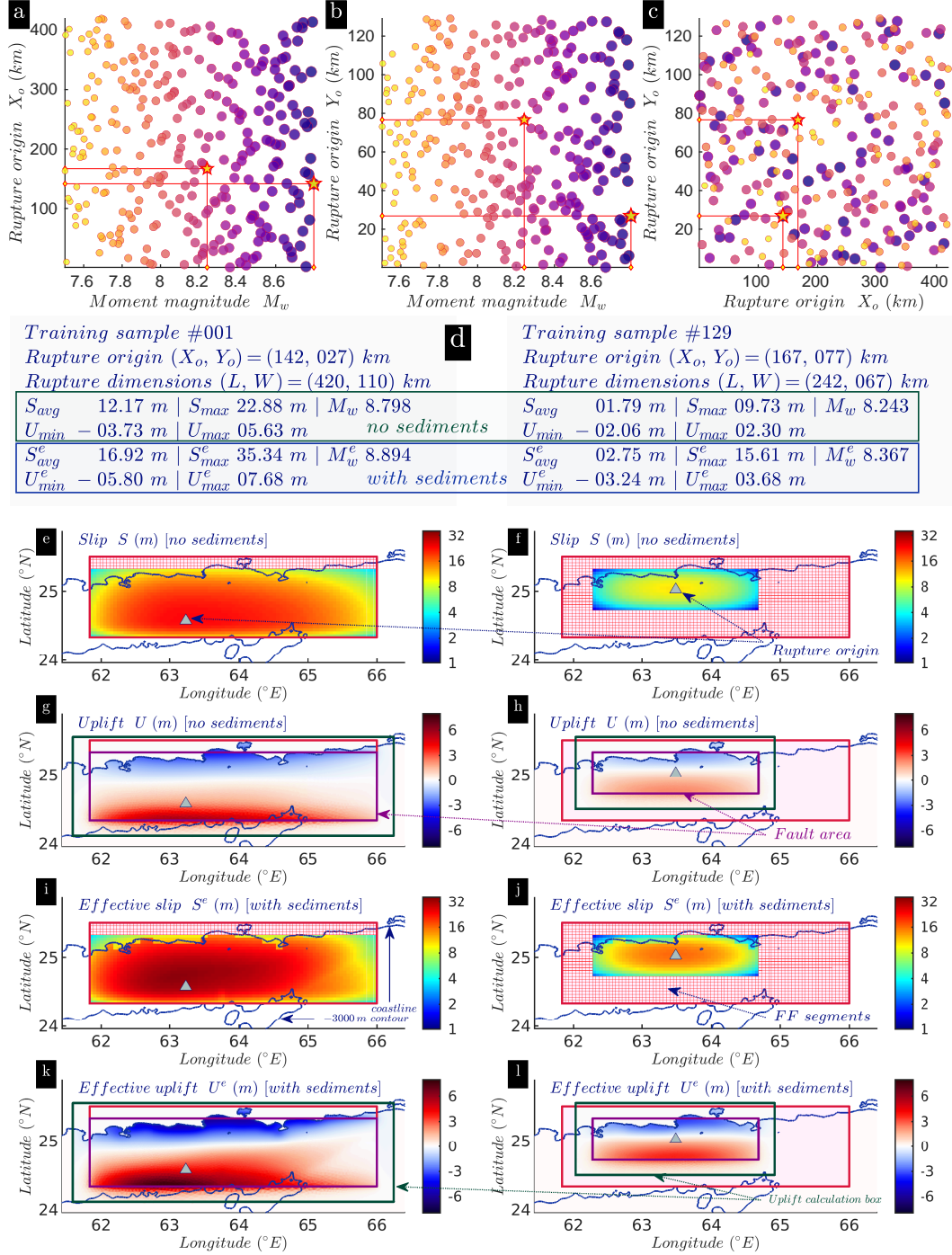
361 where  $n_h = \lambda_n / h_\lambda(b) = 10$  is the number of triangles in one wavelength  $\lambda_n$ . At the shore  
 362 (*i.e.*  $b = 0$ ), a minimum mesh size  $h_m$  of 500 m is specified. In the vicinity of the port,  
 363 the mesh size  $h_m^p$  is fixed as 10 m. We also fix the maximum triangle size ( $h_M$ ) as 25 km  
 364 for regions that are deep inland. Further details and construction process for onshore  
 365 and port mesh sizing functions are elaborated in Appendix C. After feeding the mesh  
 366 sizing function (Figure 7c) into Gmsh, we get the computational mesh with  $\sim 2.64$  mil-  
 367 lion cells or triangles (Figure 7d). Figures 7e-g & h-j show enlarged pictures of the mesh  
 368 at increasingly fine scales for regions with (Pasabandar port) and without (Karachi port)  
 369 local refinement respectively.

370 The outputs  $v_{max}$  and  $\eta_{max}$  for two training samples, no. 1 and 129 are plotted  
 371 in Figure 8. The figures also contains snapshots taken at various time instants during  
 372 the simulation.

## 373 2.5 Emulator Construction

374 The numerical simulation of the tsunami life cycle, *i.e.* its generation, propagation  
 375 and inundation at fine mesh resolutions is computationally expensive due to non-linearity,  
 376 and typically consumes hours on supercomputers. This is all the more prohibitive for  
 377 a probabilistic quantification since thousands of runs of the forward model are required  
 378 to adequately capture the various plausible scenarios. Statistical surrogates (or emula-  
 379 tors) provide a computationally cheap approximation of the complex tsunami solvers,  
 380 together with estimates of uncertainties in these predictions. In this study, the three in-  
 381 put model parameters are moment magnitude ( $M_w$ ) and rupture origin co-ordinates ( $X_o, Y_o$ )  
 382 (Figure 3 inset). The inputs are transformed into effective seafloor displacements (Sec-  
 383 tions 2.1, 2.2 & 2.3). The consequent tsunamis are propagated till Karachi port (Sec-  
 384 tion 2.4). The outputs of interest in our case are the maximum wave height ( $\eta_{max}$ ) and  
 385 maximum wave velocity ( $v_{max}$ ) at  $n_G$  (193) virtual gauge locations around the port.

396 Thus, the computer code (denoted by  $\mathbb{M}$ ) simulates a multi-physics two-stage phys-  
 397 ical model, *i.e.* from slips  $S^e$  to deformation  $U^e$ , then from  $U^e$  to tsunami outputs  $v$  and  
 398  $\eta$ . A design of computer experiments is an essential stage to create the data set used to  
 399 construct the emulator. This consists of evaluations of the model (or computer runs of  
 400  $\mathbb{M}$ ) at a finite number of locations in the space of input model parameters, together called  
 401 the training set. We employ a Latin Hypercube Design (LHD) of size 300 for 3 param-  
 402 eters (Figures 9a-c). This is large enough to capture complex nonlinear combined sen-  
 403 sitivities to the input parameters (*e.g.*, the influence of size and location in small and  
 404 mid-size events closer to Karachi, or large regional variations in spatial distributions of  
 405 slips), but still fits within our computational budget. The Gaussian Process (GP) em-  
 406 ulator (denoted by  $\mathcal{M}$ ) interpolates across the input-output points in the training set,  
 407 and generates uncertain predictions elsewhere in the space of input parameters. The un-  
 408 certainty in the predictions is modeled by a normal distribution whose mean and stan-  
 409 dard deviation are calculated using the Kriging formula (mean quantities denoted by  $\bar{v}_{max}$



386

387 **Figure 9.** Training set of 300 scenarios of  $(M_w, X_o, Y_o)$  generated by Latin Hypercube Design.  
 388 a) Training set projected on  $M_w - X_o$  plane. Sample nos. 1 and 129 are marked with stars.  
 389 b) Same as (a) but on  $M_w - Y_o$  plane. c) Same as (a) but on  $X_o - Y_o$  plane. d) Comparison of  
 390 relevant quantities for sample nos. 1 and 129. e) Slip  $S$  for sample no. 1 before incorporation  
 391 of sediment influence, plotted on  $\log_2$  scale. f) Same as (e) but for sample no. 129. g) Offshore  
 392 deformation  $U$  due to slip  $S$  for sample no. 1. h) Same as (g) but for sample no. 129. i) Effective  
 393 slip  $S^e$  for sample no. 1 after incorporation of sediment influence. j) Same as (i) but for sam-  
 394 ple no. 129. k) Effective deformation  $U^e$  due to slip  $S^e$  for sample no. 1. l) Same as (k) but for  
 395 sample no. 129.

and  $\bar{\eta}_{max}$ ). Derivations and exact equations can be found in Section 2 of Beck and Guillas (2016, Eqn. 2.4). GP emulation has been instrumental in successfully quantifying uncertainties in tsunami heights generated by landslides over the North Atlantic and the Western Indian Ocean as well as earthquakes over Cascadia (Salmanidou et al., 2017; Guillas et al., 2018; Salmanidou et al., 2019).

Maximum velocity magnitudes (and heights) are positive. In order to respect this physical constraint and not predict negative velocities (and heights), we feed the logarithm of  $v_{max}$  (and  $\eta_{max}$ ) into the construction of the emulator. Since the constructed emulator is now in the logarithmic scale, we transform the predicted quantities back to the original scale by accounting for the lognormal nature of the predicted distributions. Hence, the confidence intervals for the predictions, representing uncertainties, are all rendered positive, and naturally skewed in that direction, see Figure 10. Once the emulator is constructed, it needs to be validated before employing it for predictions. We turn to this aspect in the next section.

## 2.6 Emulator Diagnostics

In order to validate the quality of the emulation, we provide Leave-one-out (L-O-O) diagnostics here. As described in Section 2.5, our training set consists of 300 pairs of input-output quantities. In L-O-O, a reduced training set of 299 pairs is employed to build an emulator, which is then used to predict the output at inputs in the 1 pair that was left out. The predicted output (and its uncertainty) is compared to the actual output in the left out pair. This procedure is repeated 300 times to cover all the pairs in the training set. These tests are passed by the emulator, as seen for predicted  $\bar{v}_{max}$  in Figures 10a-f and  $\bar{\eta}_{max}$  in Figures 10g-l. The comparison between the mean of predictions from the emulator  $\mathcal{M}$  and the training data from the tsunami simulator  $\mathbb{M}$  shows that the emulator approximates well the simulator. The vertical line segments connects the predicted means with the counterpart in the training data. More importantly, the uncertainties in the predicted mean, quantified in the form of 90% prediction intervals (green bars in Figure 10), represent well the uncertainties about these predictions (or are even slightly conservative) since around 90% or more of the outputs from the training set fall within these intervals.

## 2.7 Emulator Predictions

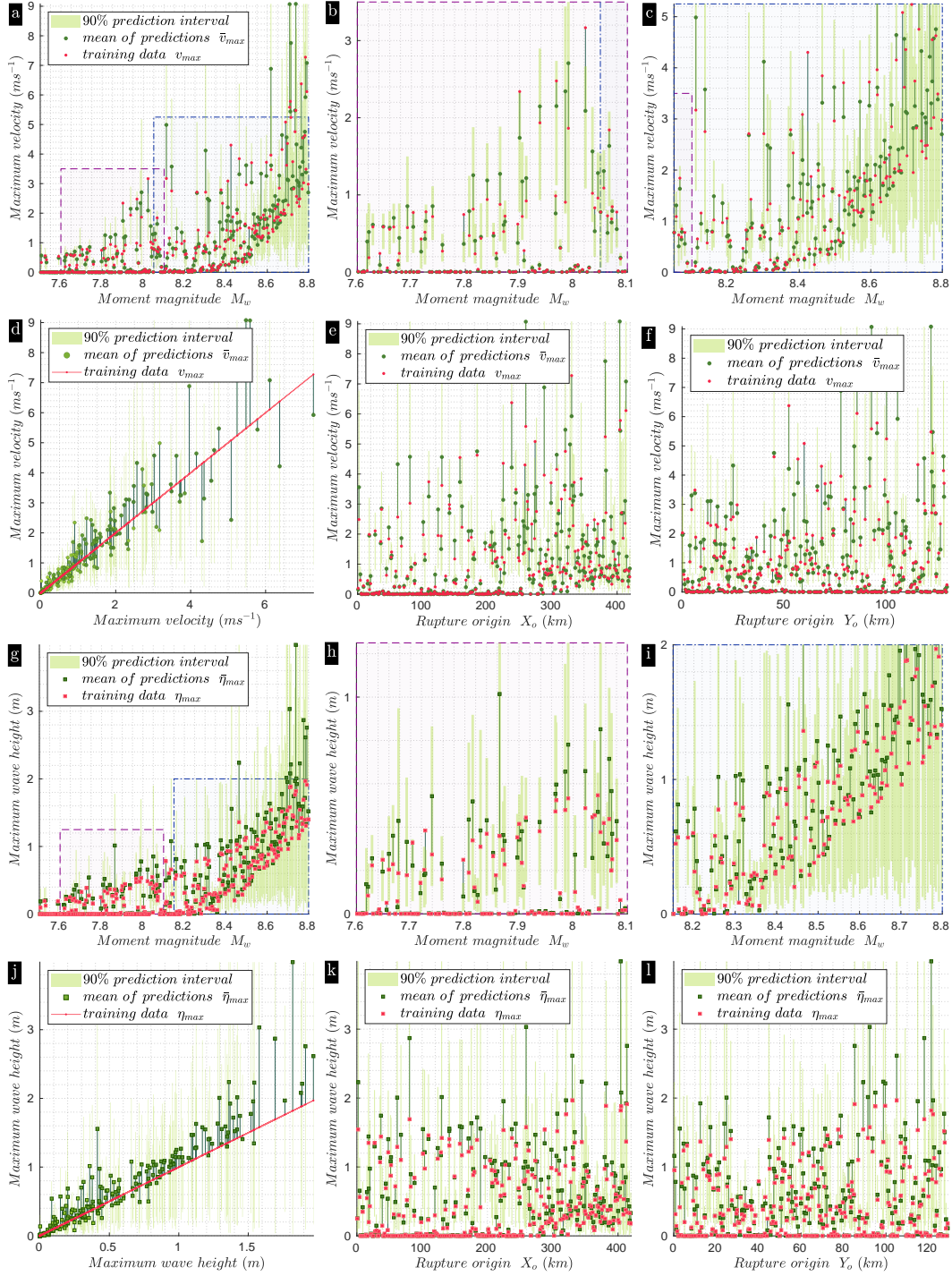
Although the 300 simulations by itself may be considered to generate a good description of the hazard, a large number of scenarios are essential for a comprehensive probabilistic hazard assessment. Thus, we evaluate the model at  $n_P$  (1 million) values of  $(M_w, X_o, Y_o)$  at 193 virtual offshore gauges (locations shown in Figure 12). The constructed emulator is used to evaluate the model at inputs that are different from those in the training set. These evaluations are termed predictions. A prediction returns the mean value of the emulated quantity and a measure of inherent statistical error/uncertainty in the approximation, *e.g.* the standard deviation. Cumulatively, these 193 million predictions not only comprehensively cover the geography around Karachi port, but also exhaustively sweep through the entire range of events in the magnitude-frequency distribution. Additionally, such a high number of samples is also needed to thoroughly explore the interplay among the three parameters in the input space of  $(M_w, X_o, Y_o)$ .

The 1 million  $M_w$  values are sampled from the Gutenberg-Richter (G-R) distribution for the MSZ. Here, the probability distribution function (pdf) for the G-R relation is modeled as the doubly truncated exponential distribution (Cosentino et al., 1977):

$$G(m) = \begin{cases} \frac{\beta e^{-\beta(m-M_w^m)}}{1 - e^{-\beta(M_w^M - M_w^m)}} & M_w^m \leq m \leq M_w^M \\ 0 & m > M_w^M \end{cases} \quad (15)$$

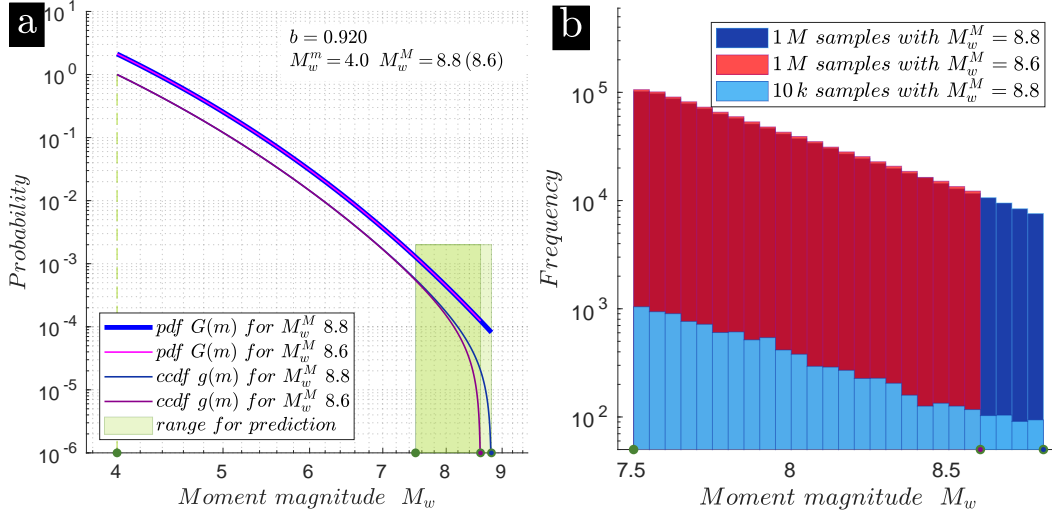
where  $\beta = b \log_e 10$  and the lower  $M_w^m$  and upper  $M_w^M$  limits of truncation are 4 and 8.8 respectively. This rate parameter  $b$  of 0.92 specific to the MSZ is taken from the most





440

441 **Figure 10.** Emulator diagnostics. a) L-O-O for emulation of maximum velocity  $v_{max}$  at a  
 442 gauge in Karachi port (gauge no. 91 in Figures 12a-b). The vertical line segments connect the  
 443 training data to its predicted counterpart. b) Enlargement of lower moment magnitude region  
 444 in (a). c) Enlargement of higher moment magnitude region in (a). d) Same data in (a) plotted  
 445 to show trend of predicted  $\bar{v}_{max}$  with respect to training  $v_{max}$ . e) Same data in (a) but plotted  
 446 with respect to  $x$ -coordinate of rupture origin  $X_o$ . f) Same data in (a) but plotted with respect  
 447 to  $y$ -coordinate of rupture origin  $Y_o$ . g-l) Same as (a)-(f) but L-O-O for emulation of maximum  
 448 height  $\eta_{max}$  at gauge no. 91.



488

489 **Figure 11.** Emulator predictions. a) The Gutenberg-Richter (G-R) relation for the MSZ,  
 490 showing probability and complementary cumulative distribution functions for two maximum mo-  
 491 ment magnitude assumptions, *viz.* 8.6 and 8.8. b) Histograms of 1 million (and 10,000)  
 492 samples of  $M_w$  used as inputs for predictions.

468 recent Earthquake Model of Middle East (EMME) database (Danciu et al., 2018, Ta-  
 469 ble S1). The complementary cumulative distribution function (ccdf), also called proba-  
 470 bility of exceedance or survival function is then:

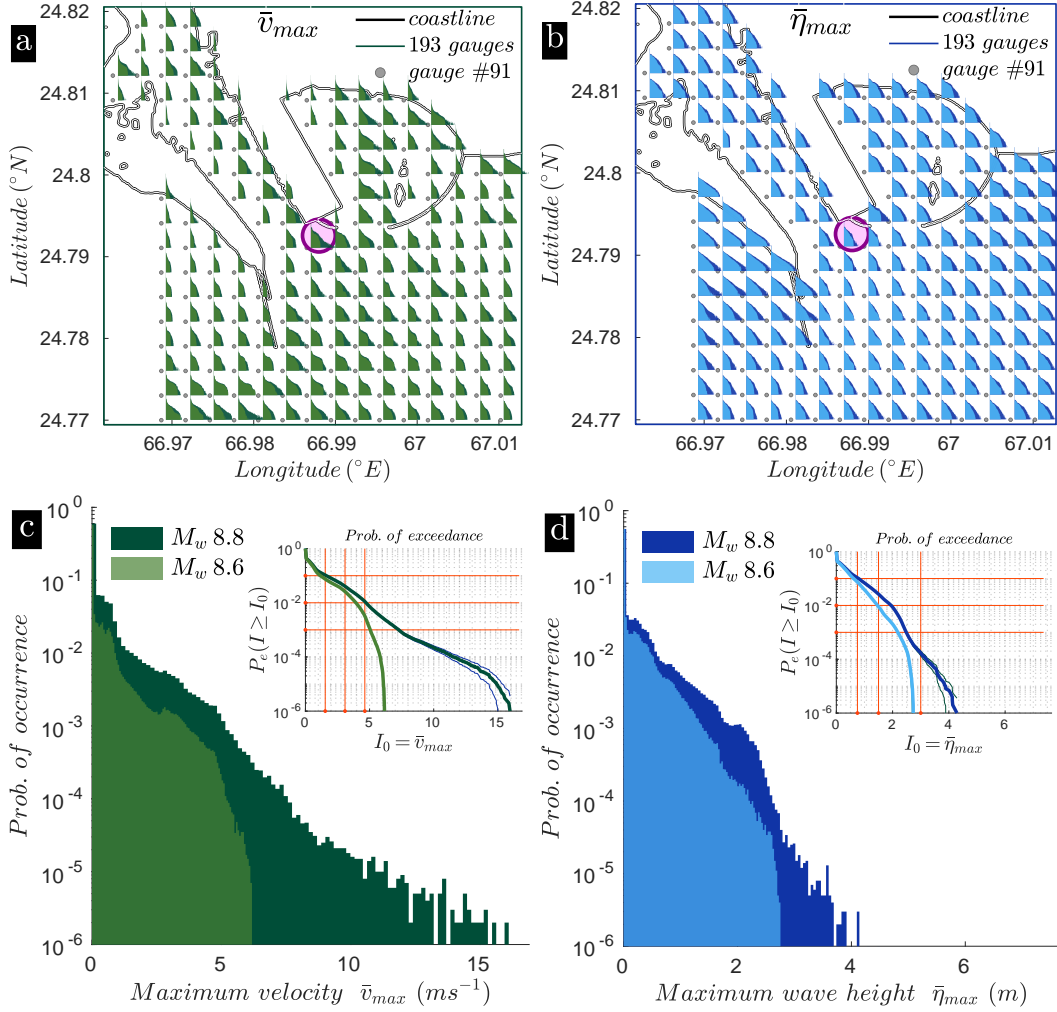
$$471 \quad g(m) = \begin{cases} 1 - \frac{1 - e^{-\beta(m - M_w^m)}}{1 - e^{-\beta(M_w^M - M_w^m)}} & M_w^m \leq m \leq M_w^M \\ 0 & m > M_w^M \end{cases} \quad (16)$$

472 The  $M_w$  for the 1 million events are then obtained by sampling the truncated distribu-  
 473 tion within our region of interest, *i.e.*  $M_w$  7.5 to  $M_w$  8.8 (see Figure 11a). The 1 million  
 474 values of  $(X_o, Y_o)$  are sampled from a uniform distribution defined over the rectangle  
 475  $[0 L^{max}] \times [0 W^{max}]$  of area  $420 km \times 129 km$ . Assuming a reduction of maximum mag-  
 476 nitude  $M_w^M$  from 8.8 to 8.6 gives a perturbed G-R relation (Figure 11a). In this case,  
 477 the 1 million samples come from the range  $M_w$  7.5 to  $M_w$  8.6. The histograms of 1 mil-  
 478 lion samples for  $M_w$  are shown in Figure 11b. It also shows 10,000 samples from the range  
 479  $M_w$  7.5 to  $M_w$  8.8 for performing comparisons.

480 To be able to generate 1 million predictions, we employ the efficiently implemented  
 481 Multiple-Output Gaussian Process emulator (MOGP) from the Alan Turing Institute.  
 482 Once the predictions are finished, we are left with two histograms (one each for  $\bar{v}_{max}$  and  
 483  $\bar{\eta}_{max}$ ) at every virtual gauge, each made up of 1 million samples of predicted quantity.  
 484 The histograms are processed to extract  $P_e(I(\mathbf{x}) \geq I_0)$ , the probability of exceedance.  
 485  $P_e$  is the probability of the tsunami having  $I(\mathbf{x}) \geq I_0$  at a gauge  $\mathbf{x}$ . The intensity  $I$  is  
 486 the measure of hazard, *i.e.* either  $\bar{v}_{max}$  or  $\bar{\eta}_{max}$ , and  $I_0$  is the intensity threshold for the  
 487 hazard quantity under consideration.

### 493 3 Results and Discussion

494 We first plot the raw output from the 1 million predictions, *i.e.* the histograms at  
 495 193 gauges in Figures 12a-b. At each gauge, two histograms are superimposed on each  
 496 other. These correspond to the two G-R relations with varying maximum moment mag-  
 497 nitude assumptions, *i.e.*  $M_w^M$  8.6 and  $M_w^M$  8.8 (Figure 11). The histograms also act as  
 498 visual indicators for the measure of the hazard at the gauge, and will be cast as hazard



505

506 **Figure 12.** Raw output from 1 million predictions at 193 gauges. a) Histograms of 1 million  
 507 predicted maximum velocities  $\bar{v}_{max}$  at each of the 193 gauges. Each histogram has the same scale as (c). Histograms from maximum moment magnitude of 8.8 and 8.6 are superimposed. b) Same  
 508 as (a) but for predicted maximum heights  $\bar{\eta}_{max}$ . c) Enlarged normalized histograms of predicted  
 509 maximum velocities at gauge no. 91 comparing the two cases of different maximum moment mag-  
 510 nitude. Inset shows probability of exceedance curves extracted from the histograms, with 99%  
 511 confidence interval. d) Same as (c) but for predicted maximum heights.

499 maps in Figure 14. Near the tip of breakwaters and the mouth of the harbor, we observe  
 500 relatively higher velocities than in other regions. We also observe a complementary re-  
 501 lation between the histograms of velocities and wave heights: the gauges having thicker  
 502 histograms for velocity have thinner histograms for wave heights and *vice versa*. These  
 503 phenomena can also be observed in the snapshots in Figure 8 (compare panels (b) & (c)  
 504 with (h) & (i) respectively).

513 As expected, there is a clear reduction of hazard when the maximum moment mag-  
 514 nitude is reduced. For closer inspection, we enlarge the normalized histograms at gauge  
 515 no. 91 in Figures 12c-d. Gauge no. 91 is located in the center of the map near the mouth  
 516 of the port and is chosen since there is substantial spread of both maximum velocities  
 517 and wave heights in its histograms. In Figure 12c, the normalized histograms for max-

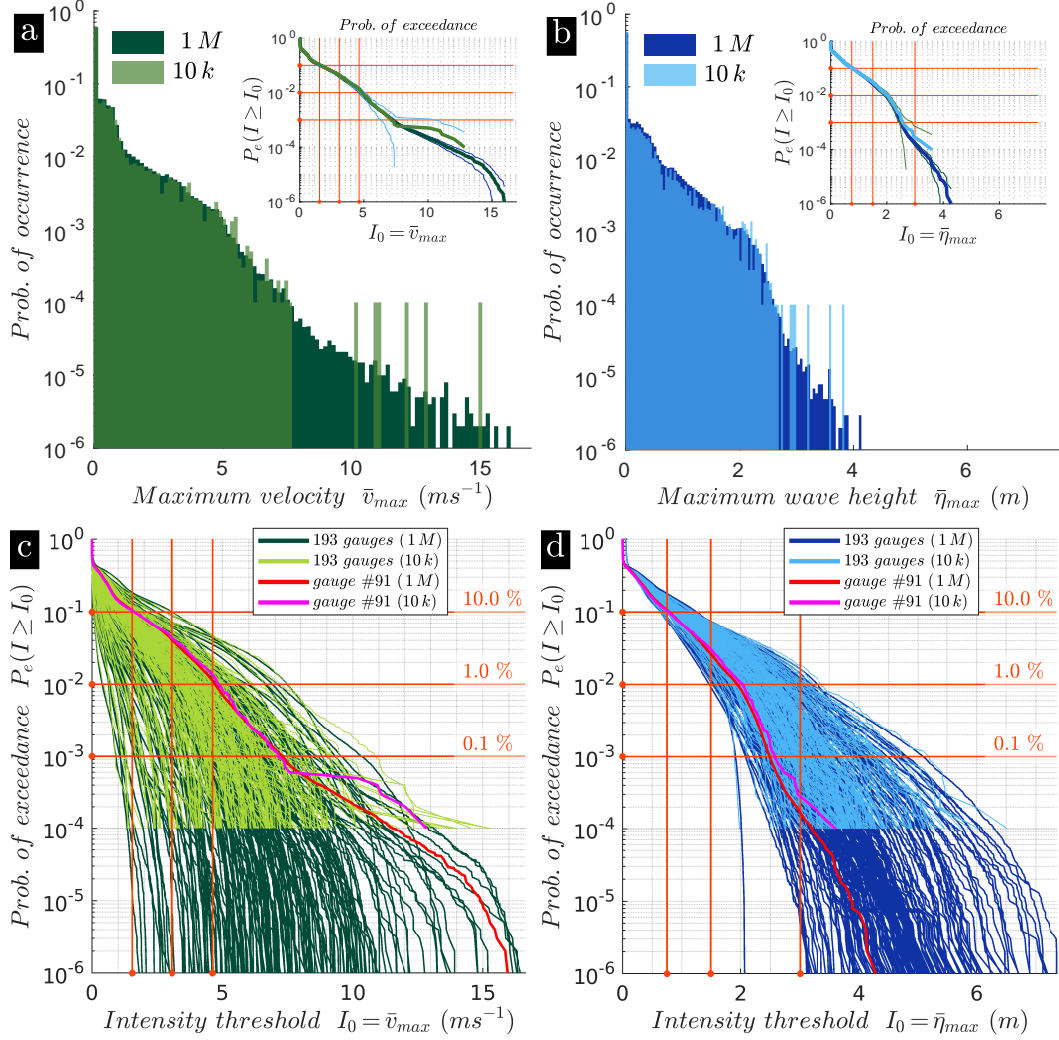
imum velocity are plotted. The range of velocities for  $M_w$  8.8 extends till  $\sim 16 \text{ m s}^{-1}$ , while it extends to only  $\sim 6.2 \text{ m s}^{-1}$  for  $M_w$  8.6. Thus, we observe a  $\sim 61 \%$  reduction in maximum velocity hazard for a  $M_w$  0.2 reduction in maximum moment magnitude. In comparison, for the same reduction in maximum moment magnitude, the reduction in hazard from maximum wave height is only  $\sim 38 \%$  (from  $\sim 4.5 \text{ m}$  to  $\sim 2.8 \text{ m}$  in Figure 12d). The probability of exceedance  $P_e$  that is extracted from the histograms is plotted in the inset of the respective figure.

Figures 13a-b compare normalized histograms for 1 million and 10,000 samples of input parameters (see Figure 11b). The corresponding probability of exceedance  $P_e$  plots with their 99% confidence intervals can be seen in the inset. In Figure 13a, we observe that the histogram corresponding to 10,000 predictions is curtailed around  $7.5 \text{ m s}^{-1}$  and becomes very sparse for higher velocities. This is due to a deficit of samples that results in the isolated bars for higher velocities. This behaviour also translates into larger uncertainties (or wider confidence intervals) for estimates of low probabilities of  $P_e$ . In contrast, 1 million predictions adequately sweep through the entire range of velocities resulting in lower uncertainties (or narrower confidence intervals) for the tail probabilities. It may be noted that tail probabilities in the  $P_e$  curve correspond to extreme events with higher velocities. Similar behaviour is seen in Figure 13b, where the deficit of samples is observed for maximum wave heights higher than  $2.7 \text{ m s}^{-1}$  for the case of 10,000 predictions.

In Figures 13c-d, we plot the probability of exceedance curves extracted from the histograms of 1 million predictions for the 193 gauges. Superimposed on top are the  $P_e$  curves for 10,000 predictions. The horizontal lines in the plots are the chosen values of probability of exceedance,  $10^{-1}$ ,  $10^{-2}$  and  $10^{-3}$ , progressively decreasing by an order of magnitude. The vertical lines in Figure 13c denote maximum velocities of 1.5, 3.1 and  $4.6 \text{ m s}^{-1}$  (or 3, 6 and 9 knots respectively), values that demarcate categories of damage in Figure 1 of Lynett et al. (2014). The vertical lines in Figure 13c denote maximum wave heights of 0.75, 1.5 and  $3 \text{ m}$ . These values are used to construct hazard maps in Figure 14. In both Figures 13c-d, the reach of the  $P_e$  curve is extended beyond the low probability of  $10^{-4}$  to include even extreme events only in the case of 1 million predictions. Additionally, although the lower probabilities (around  $10^{-4}$ ) have been made accessible by 10 thousand events, they require 1 million events for accurate resolution: with only 10,000 samples, both probabilities and quantities are overestimated between  $10^{-3}$  and  $10^{-4}$ . Hence, being able to produce a very large number of predictions is crucial to hazard assessment. Only with the utilization of the emulator – needing only 300 simulations – are we able to afford realistic predictions of velocities and wave heights at high resolution.

Port hazard maps were developed for Crescent City, California (Lynett et al., 2014) and four sites in New Zealand (Borrero, Goring, et al., 2015). The hazard was represented on the maps by velocity zonations, a time-threshold metric and safe depths for vessel evacuation. Here, the probability of exceedance curves in Figure 13 are cast as hazard maps in Figure 14, more along the lines of Gonzalez et al. (2013). We plot the probability of exceedance at the 193 gauges on the map for the chosen values of maximum velocities in Figures 14a-c. Similar plots for chosen values of maximum wave heights are shown in Figures 14d-f. For both velocities and wave heights, the overall probability decreases as the intensity threshold increases. Specifically, the bulk of  $P_e$  for maximum velocities is concentrated at the tip of breakwaters and along the dredged channel leading into the port (seen in port bathymetry, Figure 6j), as also observed in (Lynett et al., 2012). This is also supported by the patterns of localised higher maximum velocities in Figures 8a & d. In contrast, the spatial distribution of  $P_e$  for maximum wave height shows a complementary behaviour and is more spread out.

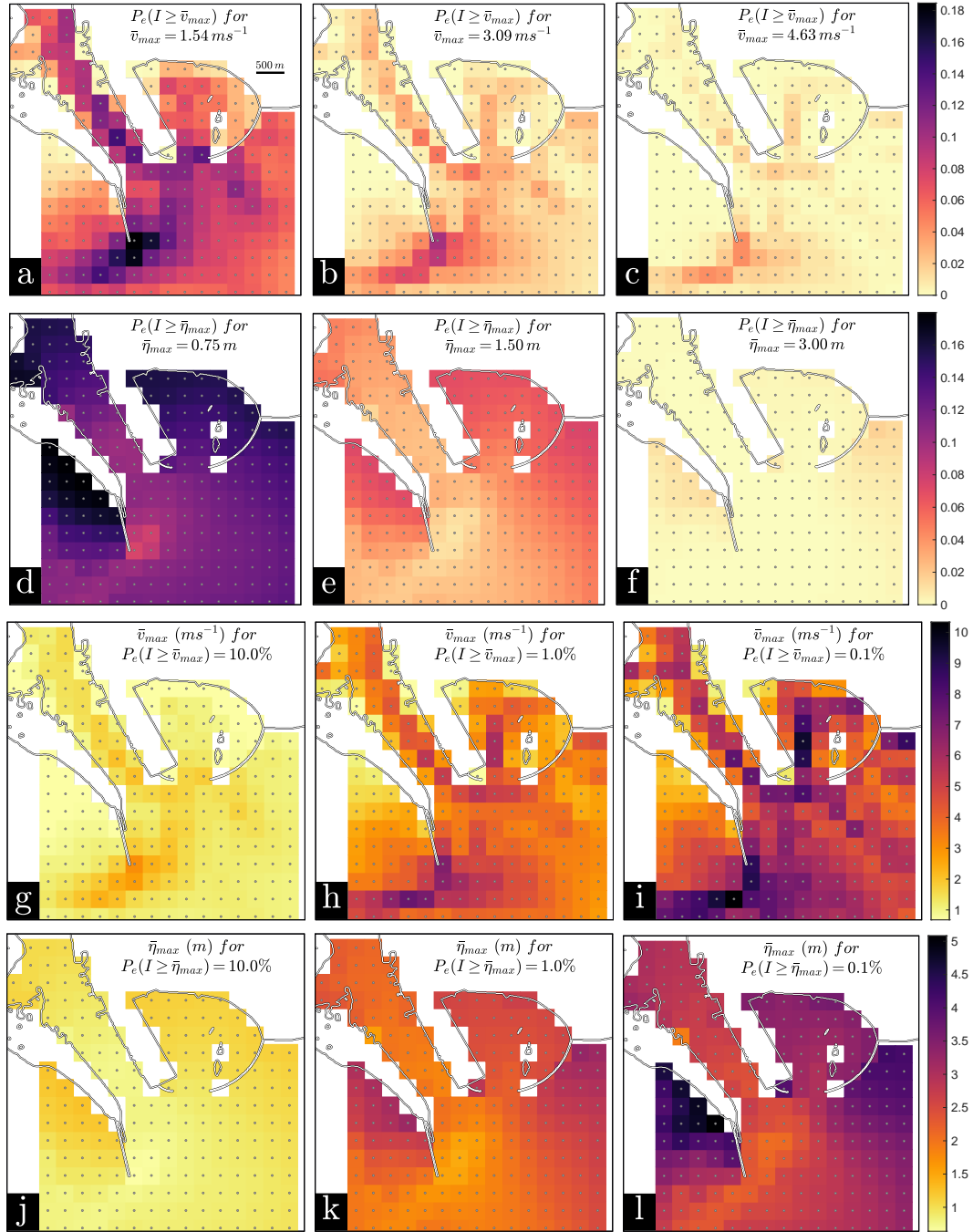
Conversely, for chosen probabilities of exceedance, the corresponding hazard thresholds at the gauges are plotted in Figures 14g-l. As expected, the overall intensity thresholds increase with decrease in probability of exceedance. Again, the bulk of the maxi-



525

526 **Figure 13.** Hazard curves. a) Comparison of normalized histograms of 1 million and 10,000  
 527 predicted maximum velocities  $\bar{v}_{max}$  at gauge no. 91. Inset shows probability of exceedance curves  
 528 extracted from the histograms, with 99% confidence intervals. b) Same as (a) but for predicted  
 529 maximum heights  $\bar{\eta}_{max}$ . c) Probability of exceedance curves for predicted maximum velocities  
 530 at 193 gauges. The curves for 10,000 predictions are superimposed over those from 1 million  
 531 predictions. Curves for gauge no. 91 are marked out. Chosen values of probabilities and intensity  
 532 thresholds used to generate hazard maps are marked as horizontal and vertical lines respectively.  
 533 d) Same as (c) but for predicted maximum wave heights.





578

579 **Figure 14.** Hazard maps. a-c) Probability of exceedance at the 193 gauges for three chosen  
 580 values of predicted maximum velocities  $\bar{v}_{max}$ . d-f) Predicted maximum velocities for three given  
 581 probabilities of exceedance. g-l) Same as (a)-(f) but for predicted maximum wave heights  $\bar{\eta}_{max}$ .

585 mum velocity threshold is concentrated at the tip of breakwaters and along the dredged  
 586 channel (Figures 14g-i). Here too, we see a complementary behaviour for maximum wave  
 587 height in Figures 14j-l.

588 Arcos and LeVeque (2015) found that velocities have more spatial variation than  
 589 heights. Dengler and Uslu (2011) showed increased sensitivity of velocities to port con-  
 590 figurations, compared to wave heights. The larger spatial variation of velocities in Fig-  
 591 ure 13c compared to wave heights in Figure 13d is evident in the probability of exceedance  
 592 plotted for all the gauges. This can be attested in Figures 12a-b, where the bulkiness of  
 593 velocity histograms varies spatially much more than that of the heights. Additionally,  
 594 at a given gauge, we observe that the spread of velocities is much more than those of the  
 595 heights for the same set of earthquake scenarios, *e.g.* compare Figures 12a-b for gauge  
 596 no. 91. These behaviours can also be deduced for individual runs from the spatial vari-  
 597 ations of maximum velocity and wave height in Figure 8 (compare panels (a) & (d) with  
 598 (g) & (j) respectively).

599 The probability of exceedance extracted in this work acts as the basic input for com-  
 600 mon hazard outputs of probability of occurrence (and return periods), especially the  $\sim 2475$   
 601 year mean return period for the Maximum Considered Tsunami (MCT) as laid out in  
 602 Chapter 6 of ASCE 7-16 (Chock, 2016). It also feeds into loss estimation functions (Muhari  
 603 et al., 2015). But a full probabilistic assessment would ideally need to include further  
 604 sources of uncertainties. These include layers of uncertainties that are either epistemic  
 605 or aleatoric in nature. Epistemic uncertainties include the scaling relation, and the Gutenberg-  
 606 Richter approximation of the occurrence-magnitude relationship (Davies et al., 2018),  
 607 *i.e.* both the maximum moment magnitude and the  $b$ -value. The major influence of the  
 608 maximum magnitude was illustrated in initial work by Hoechner et al. (2016), but for  
 609 a simplified tsunami modeling strategy. Here, we only assess two cases, for  $M_w^M$  8.6 and  
 610  $M_w^M$  8.8. Uncertainties in the bathymetry near shore have also been shown to have a large  
 611 influence on tsunamis at the shore (Liu & Guillas, 2017). Combining the tools of dimen-  
 612 sion reduction and emulation, such a modeling of the epistemic uncertainty would be ben-  
 613 efiticial to include.

614 Aleatoric uncertainties in the variations of the geometry in the seafloor uplift and  
 615 subsidence can be readily incorporated. An alternative to our slip profile generation is  
 616 to directly parameterize the co-seismic deformation profile using 3 parameters as in Guillas  
 617 et al. (2018) (or more) to vary the geometry more freely and be more realistic. The Okada  
 618 model that transforms the slips to the vertical deformation is then bypassed. This route  
 619 is quite attractive since it allows the creation of very realistic deformation patterns with  
 620 a fixed number of parameters, and does away with the dependency of the deformation/slip  
 621 on the resolution of the segmentation (shown in Figure 3b inset).

622 Our work uniformly samples the 1 million samples for rupture origin co-ordinates  
 623 (another aleatoric uncertainty). However, a recent spatial distribution of locking has been  
 624 made available for the MSZ (Frohling & Szeliga, 2016). It would be even more realis-  
 625 tic to sample the rupture origin coordinates using the locking distribution, since zones  
 626 of high locking act as a major cause for earthquake reoccurrence as recently hypothesised  
 627 in Moernaut et al. (2018). The locations could be further distributed based on the depth  
 628 dependent rigidity (Scala et al., 2019).

629 Randomness in tide levels at the time of impact (consequent changes of up to 25%  
 630 reported in Ayca and Lynett (2016)) could be included, as well as the numerical error  
 631 in the approximation of the currents since our depth-averaged model is 2-D but 3-D mod-  
 632 eling will increase precision, and account for vertical vorticity (Lynett et al., 2017; Lynett,  
 633 2016). Better designs of computer experiments than the Latin Hypercube Design used  
 634 here could be employed to reduce uncertainties in the emulator’s approximation, such  
 635 as sequential design (Beck & Guillas, 2016) already used for tsunamis with success and  
 636 is now implemented in an advanced computational workflow.

637 Instead of investigating a range of scenarios, if one only wants to examine the max-  
 638 imum wave height in order to build defences for instance, a recent surrogate-based op-  
 639 timization could be pursued whereby the design of experiment is combined with a search



640 for the maximum, saving large quantities of computational time and increasing accuracy  
 641 due to the focus on the optimization (Mathikolonis et al., 2019). To be able to emulate  
 642 a sequence of multiple models of seabed deformation and tsunami propagation, and possi-  
 643 bly a 3-D model of currents locally, a new approach, called integrated emulation (Ming  
 644 & Guillas, 2019) allows even better designs where the most influential models are run  
 645 more times where it matters, and where the integrated emulator propagates uncertain-  
 646 ties with higher fidelity by taking into account the intermediate models in the system  
 647 of simulators. This approach has the potential to enable fully realistic end-to-end cou-  
 648 pling of 3-D earthquake sources models with tsunami models (Ulrich et al., 2019).

## 649 4 Conclusions

650 In this paper, we provide a novel end-to-end quantification of uncertainties of fu-  
 651 ture earthquake-generated tsunamis heights and currents in the MSZ:

- 652 1. We replace the complex, expensive high-resolution tsunami simulator by a func-  
 653 tionally simple, cheap statistical emulator trained using 300 tsunami simulations  
 654 at 10 m mesh resolution in the vicinity of the port. We propagate uncertainties  
 655 from the Gutenberg-Richter relation to tsunami impacts of maximum velocities  
 656 and wave heights in the port area of Karachi, Pakistan. We observe maximum (ex-  
 657 treme event) velocities and wave heights of up to  $16 \text{ ms}^{-1}$  and 8 m respectively  
 658 for the range  $M_w$  7.5 – 8.8 (Figure 12).
- 659 2. We perform the largest emulation using 1 million predictions/source scenarios. To  
 660 our knowledge, this is the first large-scale uncertainty quantification of earthquake-  
 661 generated tsunami current hazard. We are able to display the necessity of this very  
 662 large number of predictions for resolving very low probabilities of exceedance ( $< 10^{-3}$ )  
 663 - very high impact extreme events ( $v_{max} > 7.5 \text{ ms}^{-1}$  and  $\eta_{max} > 3 \text{ m}$ ) with tighter  
 664 uncertainties (Figure 13).
- 665 3. We observe that reduction in hazard due to a reduction in maximum moment mag-  
 666 nitude is more for velocities than wave heights. Near the mouth of the harbor, the  
 667 reduction in hazard is  $\sim 61 \%$  for maximum velocity, but only  $\sim 38 \%$  for max-  
 668 imum wave height (corresponding to a reduction in maximum moment magnitude  
 669 from 8.8 to 8.6) (Figure 13c).
- 670 4. We generate the first area-wide probabilistic hazard maps of tsunami currents from  
 671 1 million predicted scenarios at the Karachi port (Figures 14a-f). It shows pat-  
 672 terns that are geophysically meaningful and important for the next steps of dis-  
 673 aster risk reduction. We identify concentrations of high probability of exceedance  
 674 around the port for given intensity threshold (a maximum of  $\sim 18 \%$ , 10% and 4%  
 675 for 3, 6 and 9 knots respectively) (Figures 14a-c). Conversely, the same regions  
 676 also have high intensity thresholds given probability of exceedance (a maximum  
 677 of  $\sim 3.1$ , 7.5 and  $10.3 \text{ ms}^{-1}$  for 10%, 1% and 0.1% respectively) (Figures 14d-  
 678 f). Overall, without our large-scale emulation, such outputs would be impracti-  
 679 cal to produce due to computational costs.
- 680 5. We display more spatial variations for maximum velocity compared to wave heights  
 681 around the port and their complementary behaviour for the aggregate of 1 mil-  
 682 lion scenarios (Figures 8, 12, 13 and 14).

## 683 Appendix A Slip Profile Generation

684 Select the dimension ( $h_s$ ) of a FF segment based on: (i) computational effort re-  
 685 quired – increases as  $h_s$  decreases, along  $O(n_F^2) \sim O(h_s^{-2})$ , (ii) fidelity to the scaling  
 686 relation (Figure 3b inset) – earthquake dimensions are resolved to  $O(h_s)$  (Figure 3b).  
 687 We select  $h_s \sim 5 \text{ km}$ , which for the overall FF dimensions of  $L^{max} \sim 420 \text{ km}$  and  $W^{max} \sim 129 \text{ km}$   
 688 results in 2295 segments. With the segment dimension  $h_s$ , use the scaling relation to de-

689 termine the minimum  $M_w$  that can be accommodated on the FF. To resolve the slip pro-  
 690 file adequately, we require a fault to span a minimum of 4 segments in both the length  
 691 and width directions. This results in a minimum  $M_w$  of 6.32. This is sufficient as our  
 692 region of investigation starts at  $M_w^{min} = 7.5$ . For the FF model of area  $L^{max} \times W^{max}$ ,  
 693 use the scaling relation to determine the maximum  $M_w$  that can be accommodated on  
 694 the FF. We get the maximum  $M_w$  as  $M_w^{sat} = 8.65$  (Figure 3a). Since our region of in-  
 695 vestigation is till  $M_w$  8.8, for ruptures with  $M_w > M_w^{sat}$ , we saturate the slip on the fault  
 696 with  $M_w^{sat}$ . Algorithm 1 and Figures 4b-d detail the slip profile generation given the in-  
 697 put parameter  $(M_w, X_o, Y_o)$ .

---

698 **Algorithm 1** Slip profile generation

---

- 699 1: For a given earthquake moment magnitude  $M_w$ , and rupture origin co-ordinates  
 700  $(X_o, Y_o)$  (Figure 3a inset); find the rupture length  $L$  and width  $W$  from the scaling  
 701 relation. The co-ordinates have their origin as the south-west corner of the FF (Figure  
 702 3a inset).
  - 703 2: Fit the fault rectangle of size  $L \times W$  into the FF. There are two possibilities with the  
 704 rupture origin  $(X_o, Y_o)$  being located at :  
 705 (i) the centre of the fault and equidistant from the boundaries of the fault rectangle,  
 706 *i.e.* with distances  $L/2$  and  $W/2$ .  
 707 (ii) not the centre of the fault. In this case,  $(X_o, Y_o)$  is at different distances from the  
 708 boundaries of the fault rectangle.
  - 709 3: Use Eqn. 3 to construct the lobes  $\phi(x; r_E, \alpha)$  and  $\phi(x; r_W, \alpha)$  and form the bi-  
 710 lobed kernel function for fault length  $\Phi(x; r_W, r_E, \alpha)$  (Figure 4b). Similarly, form  
 711 the bi-lobed kernel function for fault width  $\Phi(x; r_N, r_S, \alpha)$  by constructing the lobes  
 712  $\phi(x; r_N, \alpha)$  and  $\phi(x; r_S, \alpha)$  (Figure 4d).  $r_E, r_W, r_N$  and  $r_S$  are the distances of earth-  
 713 quake origin from the eastern, western, northern and southern sides of the fault rect-  
 714 angle.
  - 715 4: Use Eqn. 4 to construct the tensor product  $\Phi^\otimes$  of the two bi-lobed kernel functions in  
 716 the previous step.  $\Phi^\otimes$  will entirely reside within the fault rectangle and will become 0  
 717 at its boundaries (Figure 4c).
  - 718 5: Multiply the values of  $\Phi^\otimes$  at the centres of each segment (*i.e.*  $\Phi_i^\otimes$ ) with a factor  
 719  $M_w \left( \sum_{i=1}^{n_F} \mu l_i w_i \Phi_i^\otimes \right)^{-1}$  to get the slip  $S_i$  on the segment. This normalization results  
 720 in the slips in the fault rectangle to have a combined moment magnitude of  $M_w$ .
- 

721 **Appendix B Merging Bathymetry Data from Hydrographic Chart, SRTM,**  
 722 **GEBCO and Satellite Imagery**

723 The four data sets that are used to create the merged bathymetry for computa-  
 724 tional mesh generation (Section 2.4.2) and tsunami simulations (Section 2.4) are at dif-  
 725 ferent resolutions –  $\sim 1'' \sim 30 m$  (digitized hydrographic charts and SRTM v3),  $\sim 15'' \sim 450 m$   
 726 (GEBCO 2019), and  $\sim 10 m$  (coastline features in satellite imagery from Google Earth).  
 727 The digitized chart data is available in the domain of interest (DOI)  $[66.9332, 67.0168]^\circ E$   
 728  $\times [24.7666, 24.8334]^\circ N$ . The cosine-tapered Tukey window used in the merging process  
 729 is given by:

$$730 \quad \theta(x, r_c) = \begin{cases} \frac{1}{2} \left\{ 1 + \cos \left( \frac{2\pi}{r_c} [x - r_c/2] \right) \right\} & 0 \leq x \leq \frac{r_c}{2} \\ 1 & \frac{r_c}{2} \leq x \leq 1 - \frac{r_c}{2} \\ \frac{1}{2} \left\{ 1 + \cos \left( \frac{2\pi}{r_c} [x - 1 + r_c/2] \right) \right\} & 1 - \frac{r_c}{2} \leq x \leq 1 \end{cases} \quad (B1)$$

731 where  $r_c$  is the ratio of length of cosine-taper to the total window length of 1. Shifted  
732 and dilated versions of  $\theta$  are used to create the tensor product:

$$733 \quad \Theta(x - x_p, y - y_p, d_x, d_y, r_c^x, r_c^y) = \theta\left(\frac{x - x_p}{d_x}, r_c^x\right) \otimes \theta\left(\frac{y - y_p}{d_y}, r_c^y\right) \quad (\text{B2})$$

734 where  $(x_p, y_p)$  and  $d_x \times d_y$  are co-ordinates of the centre and area of the DOI respectively,  
735 whilst  $(r_c^x, r_c^y)$  are the cosine-fractions along the length and width of the DOI. Algorithm  
736 2 and Figure 6 detail the procedure used for merging the different bathymetries.

---

737 **Algorithm 2** Merging bathymetry data

---

- 738 1: Up-sample the hydrographic chart data and GEBCO bathymetry in the DOI on a  
739 rectangular grid having a resolution of the computational mesh ( $\sim 10 m$ ) (Figures 6a  
740 & d respectively).
  - 741 2: Integrate the polygonal domains of resolved coastline features into up-sampled  
742 bathymetry by filling land areas with a positive constant ( $2 m$ ) (Figure 6b).
  - 743 3: Interpolate the SRTM data for land onto the grid. If SRTM data exists on the water  
744 area after integration of port features, discard the SRTM data there (Figure 6c).
  - 745 4: Construct tensor product of cosine-tapered Tukey windows ( $\Theta$ ) and its complement  
746  $(1 - \Theta)$  with cosine fractions  $r_c^x = r_c^y = 10\%$  (Figures 6f & 6g respectively).
  - 747 5: Multiply hydrographic chart data integrated with port coastline features and SRTM  
748 data (Figure 6c) with  $\Theta$  (Figure 6f) to get windowed merged bathymetry (Figure 6h).  
749 The data at the start of the taper is used for the tapered region.
  - 750 6: Multiply GEBCO 2019 data (Figure 6d) with  $1 - \Theta$  (Figure 6g) to get windowed  
751 GEBCO bathymetry (Figure 6i).
  - 752 7: Add windowed merged bathymetry (Figure 6h) with windowed GEBCO bathymetry  
753 (Figure 6i) to get the final merged bathymetry (Figure 6j).
- 

## 754 Appendix C Localised Non-Uniform Unstructured Mesh

755 The mesh sizing function  $h$  that is fed into Gmsh is constructed in three stages,  
756 *viz.* offshore, onshore and port regions. For offshore mesh, the design criteria is based  
757 on the bathymetry  $b$  (Figure 7a inset). Some more steps are required after the defini-  
758 tion of  $h_\lambda$  in Eqn. 14 of Section 2.4.2. The mesh sizing  $h_\lambda$  defined in Eqn. 14 may turn  
759 out to be too steep (green curve in Figure 7a), or having a high gradient with respect  
760 to the bathymetry  $b$ . A reduction in gradient is achieved by interpolating between the  
761 triangle size  $\lambda_o/n_h$  at  $b_o$  and the minimum mesh size  $h_m$  at the coast, *i.e.*  $b = 0$  (red curve  
762 in Figure 7a):

$$763 \quad h_I(b) = b(\mathbf{x}) * (\lambda_o/n_h - h_m) / (b_o - 0) + h_m \quad (\text{C1})$$

764 The mesh sizing function  $h(b)$  is then given by the minimum:

$$765 \quad h(b) = \min(h_\lambda(b), h_I(b)) \quad (\text{C2})$$

766 Next, the design criteria for the onshore mesh sizing function  $h(\pi)$  is based on the  
767 coast proximity  $\pi(\mathbf{x})$  defined as the minimum distance of a point  $\mathbf{x}$  from the coastline  
768  $\mathcal{C}$  of the merged bathymetry (Figure 7b inset):

$$769 \quad \pi(\mathbf{x}) = \min_{\mathbf{x}_c \in \mathcal{C}} \|\mathbf{x} - \mathbf{x}_c\|_2 \quad (\text{C3})$$

770 The mesh sizing function is broken into three regions, *viz.* inundation, stretch and blow-  
771 up regions (Figure 7b). In the inundation region which extends inland for a distance  $\pi_I$   
772 ( $2.5 km$ ) from the coast, the mesh size is prescribed as the minimum mesh size  $h_m$  ( $500 m$ ).  
773 Thus, the inundation region acts as a smooth transitioning region between the onshore

774 and offshore mesh. Further inland away from the inundation region, we require the tri-  
 775 angle sizes to explode quickly to the maximum mesh size  $h_M$  (25 km). This region is called  
 776 the blow-up region (from  $\pi_S$  to  $\pi_B$  in Figure 7b). Since such a transition needs to hap-  
 777 pen in a smooth manner, we introduce the stretch region between the end of the inun-  
 778 dation region and the beginning of the blow-up region (from  $\pi_I$  to  $\pi_S$  in Figure 7b). In  
 779 the stretch region the triangle size transitions from  $h_m$  to  $h_S$  (10 km). To prescribe mesh  
 780 sizes in the stretch region, we define the *size ratio*  $\rho$  ( $= 1.3$ ) to be the ratio of sizes of ad-  
 781 jacent triangle in the mesh (also called *grading gauge* in Legrand et al. (2006)). The stretch  
 782 distance  $\pi_S - \pi_I$  is calculated as:

$$783 \quad \pi_S - \pi_I = h_m + \rho h_m + \rho^2 h_m + \dots + \rho^{n_S} h_m \quad (C4)$$

784 Eqn. C4 is a geometric series that approximates the distance by summing up the sizes  
 785 of  $n_S + 1$  triangles, lined up end-to-end in a straight line, progressively increasing in size  
 786 by a factor of  $\rho$  (Legrand et al., 2006), starting from  $h_m$  to  $\rho^{n_S} h_m$ . Equating the last  
 787 term to  $h_S$ , solves for integer  $n_S$  as:

$$788 \quad n_S = \lceil \log_\rho \left( \frac{h_S}{h_m} \right) \rceil \quad (C5)$$

789 where  $\lceil \cdot \rceil$  denotes the ceiling function. Similarly, the blow-up distance  $\pi_B - \pi_S$  is cal-  
 790 culated as:

$$791 \quad \pi_B - \pi_S = h_S + \rho h_S + \rho^2 h_S + \dots + \rho^{n_B} h_S \quad (C6)$$

792 Similar to Eqn. C4, Eqn. C6 is a geometric series summing up the sizes of  $n_B + 1$  tri-  
 793 angles, progressively increasing in size from  $h_S$  to  $\rho^{n_B} h_S$ , by a factor of  $\rho$ . Equating the  
 794 last term to  $h_M$ , solves for integer  $n_B$  as:

$$795 \quad n_B = \lceil \log_\rho \left( \frac{h_M}{h_S} \right) \rceil \quad (C7)$$

796 The mesh sizing function is specified to Gmsh on a background rectangular mesh. The  
 797 resolution of the background mesh is half the resolution of GEBCO grid, *i.e.*  $\sim 210$  m,  
 798 sufficient for specifying the  $h_m$  of 500 m. Each of the above mesh sizings for the inun-  
 799 dation, stretch and blow-up regions need to be specified on the background mesh. The  
 800 number of levels mentioned in Figure 7b are the number of grids in the background mesh  
 801 needed to specify mesh sizes in the respective region.

802 Finally, the mesh sizing function is constructed in the vicinity of the port (Figure  
 803 7h-j). The strategy followed is similar to offshore mesh sizing, but instead of the prox-  
 804 imity to coast, the radial distance from the centre  $(x_p, y_p)$  of the DOI (or port) is used.  
 805 A  $\rho^p$  of 1.05 is chosen for a very smooth transition of mesh. The mesh sizing is fixed at  
 806  $h_m^p$  (10 m) for the DOI where the resolved bathymetry is available. The resolution of back-  
 807 ground mesh near the port is kept at 10 m, *i.e.* at least same as  $h_m^p$ . In increasing radii  
 808 extending outwards from the DOI, the mesh sizing increases similar to Eqn. C4 but it-  
 809 eratively with increasing number of terms. The iterative procedure is employed to en-  
 810 sure that there is a smooth merging of the mesh sizing function at the port with exist-  
 811 ing offshore and onshore mesh sizing functions.

## 812 Acknowledgments

813 MH and SG conceptualized the problem. SG and DG conceptualized the employment  
 814 of large-scale statistical emulation and the inclusion of the effect of sediments. MH dig-  
 815 itized the bathymetry from the hydrographic chart for Karachi port. DG developed the  
 816 software and related methodologies employed in this work except for those mentioned  
 817 below. DG designed the problem with inputs and supervision from SG and MH, curated  
 818 data, and carried out the simulations with associated validation, analysis and data pro-  
 819 cessing. All authors drafted and critically reviewed the manuscript.

820 DG and SG were supported by the Alan Turing Institute under the EPSRC grant  
 821 [EP/N510129/1] for the project ‘*Uncertainty Quantification of multi-scale and multiphysics*  
 822 *computer models: applications to hazard and climate models*’. DG was partially funded  
 823 by the Royal Society-SERB Newton International Fellowship [NF151483] for the project  
 824 ‘*Inverse modeling of Tsunami Source Characterization and its Use in Early Warnings*’.  
 825 DG, MH and SG acknowledge funding from the NERC grant [NE/P016367/1] ‘*Tsunami*  
 826 *risk for the Western Indian Ocean: steps toward the integration of science into policy*  
 827 *and practice*’ under the Global Challenges Research Fund: Building Resilience programme.

828 This work has been performed using resources provided by the Cambridge Tier-  
 829 2 system (CSD3 Wilkes2) operated by the University of Cambridge Research Comput-  
 830 ing Service funded by EPSRC Tier-2 capital grant EP/P020259/1. The authors would  
 831 like to acknowledge the use of the University of Oxford Advanced Research Computing  
 832 (ARC) facility (JADE) in carrying out this work (doi.org/10.5281/zenodo.22558). Prepar-  
 833 ative simulations were performed on the EMERALD High Performance Computing fa-  
 834 cility provided via the EPSRC funded Centre for Innovation (EP/K000144/1 and EP/K000136/1),  
 835 owned and operated by the e-Infrastructure South Consortium formed by the universi-  
 836 ties of Bristol, Oxford, Southampton and UCL in partnership with STFC Rutherford  
 837 Appleton Laboratory.

838 The 1'' topography was sourced from SRTM (v3) (earthexplorer.usgs.gov), and 5'  
 839 sediment thickness from GlobSed (ngdc.noaa.gov/mgg/sedthick/). Gmsh (v4.4.1) was  
 840 used for mesh generation (gmsh.info). dMODELS (v1.0) was used as a base for Okada  
 841 deformation model (pubs.usgs.gov/tm/13/b1/).

842 DG acknowledges support from Eric Daub and Oliver Strickson for active devel-  
 843 opment of MOGP UQ suite (v0.2.0) used here for statistical emulation (github.com/alan-  
 844 turing-institute/mogp\_emulator), Daniel Giles for improvements to second order FV scheme  
 845 and boundary conditions in VOLNA-OP2 (v1.5) (github.com/reguly/volna), and István  
 846 Reguly for smooth installation and running of VOLNA-OP2 on CSD3. We also acknowl-  
 847 edge fruitful discussions with Deyu Ming and Mariya Mamajiwala on truncated G-R dis-  
 848 tribution and prediction intervals for L-O-O diagnostics, Frédéric Dias on meshing strate-  
 849 gies and sediment amplification curve, Theodoros Mathikolonis on emulation, and Si-  
 850 mon Day, Kusala Rajendran and C.P. Rajendran on seismicity of MSZ.

## 851 References

- 852 Allen, T. I., & Hayes, G. P. (2017). Alternative rupture-scaling relationships for sub-  
 853 duction interface and other offshore environments. *Bulletin of the Seismological*  
 854 *Society of America*, 107(3), 1240-1253. doi: 10.1785/0120160255
- 855 Arcos, M. E. M., & LeVeque, R. J. (2015, Mar 01). Validating velocities in  
 856 the GeoClaw tsunami model using observations near Hawaii from the 2011  
 857 Tohoku tsunami. *Pure and Applied Geophysics*, 172(3), 849-867. doi:  
 858 10.1007/s00024-014-0980-y
- 859 Ayca, A., & Lynett, P. J. (2016). Effect of tides and source location on nearshore  
 860 tsunami-induced currents. *Journal of Geophysical Research: Oceans*, 121(12),  
 861 8807-8820. doi: 10.1002/2016JC012435
- 862 Battaglia, M., Cervelli, P., & Murra-Muraleda, J. (2012). Modeling crustal deformation  
 863 \_A catalog of deformation models and modeling approaches. *US Geological*  
 864 *Survey Techniques and Methods*, 37-85.
- 865 Battaglia, M., Cervelli, P. F., & Murray, J. R. (2013). dMODELS: A MATLAB soft-  
 866 ware package for modeling crustal deformation near active faults and volcanic  
 867 centers. *Journal of Volcanology and Geothermal Research*, 254, 1 - 4.
- 868 Beck, J., & Guillas, S. (2016). Sequential design with Mutual Information for Com-  
 869 puter Experiments (MICE): Emulation of a tsunami model. *SIAM/ASA Jour-  
 870 nal on Uncertainty Quantification*, 4(1), 739-766.
- 871 Blaser, L., Krger, F., Ohrnberger, M., & Scherbaum, F. (2010). Scaling relations of  
 872 earthquake source parameter estimates with special focus on subduction envi-



- ronment. *Bulletin of the Seismological Society of America*, 100(6), 2914-2926.  
doi: 10.1785/0120100111
- Borrero, J. C., Goring, D. G., Greer, S. D., & Power, W. L. (2015). Far-field tsunami hazard in New Zealand ports. *Pure and Applied Geophysics*, 172(3), 731–756. doi: 10.1007/s00024-014-0987-4
- Borrero, J. C., Lynett, P. J., & Kalligeris, N. (2015). Tsunami currents in ports. *Philosophical Transactions of the Royal Society A: Mathematical, Physical and Engineering Sciences*, 373(2053), 20140372. doi: 10.1098/rsta.2014.0372
- Byrne, D. E., Sykes, L. R., & Davis, D. M. (1992). Great thrust earthquakes and aseismic slip along the plate boundary of the Makran Subduction Zone. *Journal of Geophysical Research: Solid Earth*, 97(B1), 449-478. doi: 10.1029/91JB02165
- Chock, G. Y. K. (2016). Design for tsunami loads and effects in the ASCE 7-16 standard. *Journal of Structural Engineering*, 142(11), 04016093. doi: 10.1061/(ASCE)ST.1943-541X.0001565
- Cosentino, P., Ficarra, V., & Luzio, D. (1977, 12). Truncated exponential frequency-magnitude relationship in earthquake statistics. *Bulletin of the Seismological Society of America*, 67(6), 1615-1623.
- Danciu, L., et al. (2018, 01). The 2014 earthquake model of the Middle East: seismogenic sources. *Bulletin of Earthquake Engineering*, 16(8), 3465–3496. doi: 10.1007/s10518-017-0096-8
- Davies, G., et al. (2018). A global probabilistic tsunami hazard assessment from earthquake sources. *Geological Society, London, Special Publications*, 456(1), 219–244.
- Dengler, L., & Uslu, B. (2011). Effects of harbor modification on Crescent City, California’s tsunami vulnerability. *Pure and Applied Geophysics*, 168(6), 1175–1185. doi: 10.1007/s00024-010-0224-8
- Dias, F., Dutykh, D., O’Brien, L., Renzi, E., & Stefanakis, T. (2014). On the modelling of tsunami generation and tsunami inundation. *Procedia IUTAM*, 10, 338 - 355. (Mechanics for the World: Proceedings of the 23rd International Congress of Theoretical and Applied Mechanics, ICTAM2012) doi: doi.org/10.1016/j.piutam.2014.01.029
- Dutykh, D., & Dias, F. (2010). Influence of sedimentary layering on tsunami generation. *Computer Methods in Applied Mechanics and Engineering*, 199(21), 1268 - 1275. (Multiscale Models and Mathematical Aspects in Solid and Fluid Mechanics) doi: doi.org/10.1016/j.cma.2009.07.011
- Dutykh, D., Poncet, R., & Dias, F. (2011). The VOLNA code for the numerical modeling of tsunami waves: Generation, propagation and inundation. *European Journal of Mechanics - B/Fluids*, 30(6), 598 - 615. (Special Issue: Nearshore Hydrodynamics) doi: https://doi.org/10.1016/j.euromechflu.2011.05.005
- Frohling, E., & Szeliga, W. (2016). GPS constraints on interplate locking within the Makran subduction zone. *Geophysical Journal International*, 205(1), 67-76. doi: 10.1093/gji/ggw001
- GEBCO Bathymetric Compilation Group 2019. (2019). *The GEBCO\_2019 Grid - a continuous terrain model of the global oceans and land*. British Oceanographic Data Centre, National Oceanography Centre, NERC, UK. doi: 10/c33m
- Geuzaine, C., & Remacle, J.-F. (2009). Gmsh: A 3-D finite element mesh generator with built-in pre- and post-processing facilities. *International Journal for Numerical Methods in Engineering*, 79(11), 1309–1331. doi: 10.1002/nme.2579
- Giles, D., Kashdan, E., Salmanidou, D. M., Guillas, S., & Dias, F. (2020). Performance analysis of Volna-OP2 – massively parallel code for tsunami modelling. *arXiv preprint arXiv:2002.04889*.
- Gonzalez, F. I., LeVeque, R. J., & Adams, L. M. (2013). *Probabilistic Tsunami Hazard Assessment (PTHA) for Crescent City, CA. Final Report for Phase I*

- (Tech. Rep.). University of Washington Department of Applied Mathematics.
- 928 Grezio, A., Babeyko, A., Baptista, M. A., Behrens, J., Costa, A., Davies, G., . . .  
 929 Thio, H. K. (2017). Probabilistic tsunami hazard analysis: Multiple sources  
 930 and global applications. *Reviews of Geophysics*, *55*(4), 1158-1198. doi:  
 931 10.1002/2017RG000579
- 932
- 933 Guillas, S., Sarri, A., Day, S. J., Liu, X., Dias, F., et al. (2018). Functional emu-  
 934 lation of high resolution tsunami modelling over Cascadia. *The Annals of Ap-  
 935 plied Statistics*, *12*(4), 2023-2053.
- 936 Hanks, T. C., & Kanamori, H. (1979). A moment magnitude scale. *Journal  
 937 of Geophysical Research: Solid Earth*, *84*(B5), 2348-2350. doi: 10.1029/  
 938 JB084iB05p02348
- 939 Hasan, H., Lodhi, H., LeVeque, R., Lodhi, S., & Ahmed, S. (2017). Assessing  
 940 tsunami risk to Karachi Port through simulation of currents that were report-  
 941 edly produced there by the 1945 Makran tsunami. In *Proceedings of the 16th  
 942 world conference on earthquake engineering, santiago, chile*.
- 943 Hayes, G. P. (2018). *Slab2 - A Comprehensive Subduction Zone Geometry Model:  
 944 U.S. Geological Survey data release*. British Oceanographic Data Centre, Na-  
 945 tional Oceanography Centre, NERC, UK. doi: 10.5066/F7PV6JNV
- 946 Hayes, G. P., Moore, G. L., Portner, D. E., Hearne, M., Flamme, H., Furtney, M.,  
 947 & Smoczyk, G. M. (2018). Slab2, a comprehensive subduction zone geometry  
 948 model. *Science*, *362*(6410), 58-61. doi: 10.1126/science.aat4723
- 949 Heidarzadeh, M., & Kijko, A. (2011). A probabilistic tsunami hazard assessment for  
 950 the Makran subduction zone at the northwestern Indian Ocean. *Natural Haz-  
 951 ards*, *56*(3), 577-593. doi: 10.1007/s11069-010-9574-x
- 952 Heidarzadeh, M., Pirooz, M. D., Zaker, N. H., Yalciner, A. C., Mokhtari, M., & Es-  
 953 maeily, A. (2008). Historical tsunami in the Makran Subduction Zone off the  
 954 southern coasts of Iran and Pakistan and results of numerical modeling. *Ocean  
 955 Engineering*, *35*(8), 774 - 786. doi: doi.org/10.1016/j.oceaneng.2008.01.017
- 956 Heidarzadeh, M., & Satake, K. (2014). Possible sources of the tsunami observed in  
 957 the northwestern Indian Ocean following the 2013 September 24 Mw 7.7 Pak-  
 958 istan inland earthquake. *Geophysical Journal International*, *199*(2), 752-766.  
 959 doi: 10.1093/gji/ggu297
- 960 Hoechner, A., Babeyko, A. Y., & Zamora, N. (2016). Probabilistic tsunami hazard  
 961 assessment for the Makran region with focus on maximum magnitude assump-  
 962 tion. *Natural Hazards and Earth System Sciences*, *16*(6), 1339-1350. doi:  
 963 10.5194/nhess-16-1339-2016
- 964 Kanamori, H. (1977). The energy release in great earthquakes. *Journal of Geophysi-  
 965 cal Research (1896-1977)*, *82*(20), 2981-2987. doi: 10.1029/JB082i020p02981
- 966 Legrand, S., Deleersnijder, E., Hanert, E., Legat, V., & Wolanski, E. (2006). High-  
 967 resolution, unstructured meshes for hydrodynamic models of the Great Barrier  
 968 Reef, Australia. *Estuarine, Coastal and Shelf Science*, *68*(1), 36 - 46. doi:  
 969 https://doi.org/10.1016/j.ecss.2005.08.017
- 970 Liu, X., & Guillas, S. (2017). Dimension reduction for Gaussian process emulation:  
 971 An application to the influence of bathymetry on tsunami heights. *SIAM/ASA  
 972 Journal on Uncertainty Quantification*, *5*(1), 787-812.
- 973 Lynett, P. J. (2016). Precise prediction of coastal and overland flow dynamics:  
 974 A grand challenge or a fools errand. *Journal of Disaster Research*, *11*(4), 615-  
 975 623. doi: 10.20965/jdr.2016.p0615
- 976 Lynett, P. J., Borrero, J., Son, S., Wilson, R., & Miller, K. (2014). Assessment  
 977 of the tsunami-induced current hazard. *Geophysical Research Letters*, *41*(6),  
 978 2048-2055. doi: 10.1002/2013GL058680
- 979 Lynett, P. J., Borrero, J. C., Weiss, R., Son, S., Greer, D., & Renteria, W.  
 980 (2012). Observations and modeling of tsunami-induced currents in ports  
 981 and harbors. *Earth and Planetary Science Letters*, *327-328*, 68 - 74. doi:  
 982 doi.org/10.1016/j.epsl.2012.02.002



- 983 Lynett, P. J., et al. (2017). Inter-model analysis of tsunami-induced coastal currents.  
 984 *Ocean Modelling*, *114*, 14 - 32. doi: doi.org/10.1016/j.ocemod.2017.04.003
- 985 Mathikolonis, T., Roeber, V., & Guillas, S. (2019). Computationally efficient  
 986 surrogate-based optimization of coastal storm waves heights and run-ups.  
 987 *arXiv preprint arXiv:1910.01932*.
- 988 Ming, D., & Guillas, S. (2019). Integrated emulators for systems of computer mod-  
 989 els. *arXiv preprint arXiv:1912.09468*.
- 990 Moernaut, J., Daele, M. V., Fontijn, K., Heirman, K., Kempf, P., Pino, M., ...  
 991 Batist, M. D. (2018). Larger earthquakes recur more periodically: New in-  
 992 sights in the megathrust earthquake cycle from lacustrine turbidite records in  
 993 south-central Chile. *Earth and Planetary Science Letters*, *481*, 9 - 19. doi:  
 994 doi.org/10.1016/j.epsl.2017.10.016
- 995 Muhari, A., Charvet, I., Tsuyoshi, F., Suppasri, A., & Imamura, F. (2015). Assess-  
 996 ment of tsunami hazards in ports and their impact on marine vessels derived  
 997 from tsunami models and the observed damage data. *Natural Hazards*, *78*(2),  
 998 1309–1328. doi: 10.1007/s11069-015-1772-0
- 999 Okada, Y. (1985). Surface deformation due to shear and tensile faults in a half-  
 1000 space. *Bulletin of the Seismological Society of America*, *75*(4), 1135-1154.
- 1001 Okal, E. A., Fritz, H. M., Raad, P. E., Synolakis, C., Al-Shijbi, Y., & Al-Saifi, M.  
 1002 (2006). Oman field survey after the December 2004 Indian Ocean tsunami.  
 1003 *Earthquake Spectra*, *22*(S3), 203-218. doi: 10.1193/1.2202647
- 1004 Reguly, I. Z., et al. (2018). The VOLNA-OP2 tsunami code (version 1.5). *Geoscientific Model Development*, *11*(11), 4621–4635. doi: 10.5194/gmd-11-4621-2018
- 1005 Salmanidou, D. M., Guillas, S., Georgiopoulou, A., & Dias, F. (2017). Statistical  
 1006 emulation of landslide-induced tsunamis at the Rockall Bank, NE Atlantic.  
 1007 *Proceedings of the Royal Society A: Mathematical, Physical and Engineering*  
 1008 *Sciences*, *473*(2200), 20170026.
- 1009 Salmanidou, D. M., Heidarzadeh, M., & Guillas, S. (2019). Probabilistic landslide-  
 1010 generated tsunamis in the Indus Canyon, NW Indian Ocean, using statisti-  
 1011 cal emulation. *Pure and Applied Geophysics*, *176*(7), 3099–3114. doi:  
 1012 10.1007/s00024-019-02187-3
- 1013 Scala, A., Lorito, S., Romano, F., Murphy, S., Selva, J., Basili, R., ... Cirella,  
 1014 A. (2019, Jun 28). Effect of shallow slip amplification uncertainty on  
 1015 probabilistic tsunami hazard analysis in subduction zones: Use of long-  
 1016 term balanced stochastic slip models. *Pure and Applied Geophysics*. doi:  
 1017 10.1007/s00024-019-02260-x
- 1018 Smith, G. L., McNeill, L. C., Wang, K., He, J., & Henstock, T. J. (2013). Ther-  
 1019 mal structure and megathrust seismogenic potential of the makran subduction  
 1020 zone. *Geophysical Research Letters*, *40*(8), 1528-1533. doi: 10.1002/grl.50374
- 1021 Straume, E. O., et al. (2019). Globsed: Updated total sediment thickness in the  
 1022 world's oceans. *Geochemistry, Geophysics, Geosystems*, *20*(4), 1756-1772. doi:  
 1023 10.1029/2018GC008115
- 1024 Ulrich, T., Vater, E. H., S. Madden, Behrens, J., van Dinther, Y., van Zelst, I.,  
 1025 Fielding, E. J., ... Gabriel, A.-A. (2019). Coupled, physics-based mod-  
 1026 eling reveals earthquake displacements are critical to the 2018 Palu, Su-  
 1027 lawesi Tsunami. *Pure and Applied Geophysics*, *176*(10), 4069–4109. doi:  
 1028 10.1007/s00024-019-02290-5
- 1029 van Scheltinga, A. D. T., Myers, P. G., & Pietrzak, J. D. (2012). Mesh generation  
 1030 in archipelagos. *Ocean Dynamics*, *62*(8), 1217–1228. doi: 10.1007/s10236-012-  
 1031 -0559-z
- 1032